Journal Pre-proof

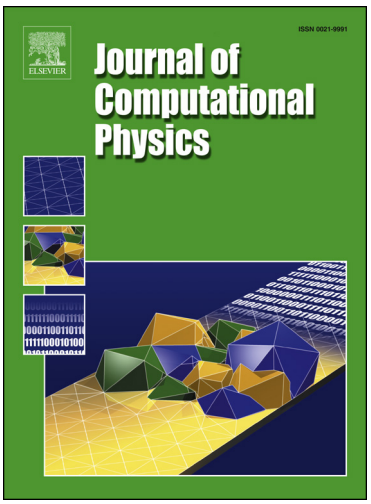

Finite volume WENO schemes for nonlinear parabolic problems with degenerate diffusion on non-uniform meshes

Todd Arbogast, Chieh-Sen Huang, Xikai Zhao

PII: S0021-9991(19)30626-6
DOI: https://doi.org/10.1016/j.jcp.2019.108921
Reference: YJCPH 108921

To appear in: *Journal of Computational Physics*

Received date: 28 February 2019
Revised date: 28 August 2019
Accepted date: 30 August 2019

Please cite this article as: T. Arbogast et al., Finite volume WENO schemes for nonlinear parabolic problems with degenerate diffusion on non-uniform meshes, *J. Comput. Phys.* (2019), 108921, doi: https://doi.org/10.1016/j.jcp.2019.108921.

Highlights

- Finite volume WENO schemes for nonlinear degenerate parabolic equations.
- Schemes applied to non-uniform computational meshes and multi-D problems.
- Explicit and implicit time evolutions are depicted.
- Stability analyses are provided.

Finite volume WENO schemes for nonlinear parabolic problems with degenerate diffusion on non-uniform meshes

Todd Arbogast[a], Chieh-Sen Huang[b], Xikai Zhao[c]

[a] *University of Texas at Austin; Oden Institute for Computational Engineering and Sciences C0200; Austin, TX 78712–1229; U.S.A.*
[b] *Department of Applied Mathematics; National Sun Yat-sen University; Kaohsiung 804; Taiwan, R.O.C.*
[c] *University of Texas at Austin; Oden Institute for Computational Engineering and Sciences C0200; Austin, TX 78712–1229; U.S.A. Currently at Schlumberger; Geophysics Technology Center (GTC); 3750 Briarpark Dr.; Houston, TX 77042; U.S.A.*

Abstract

We consider numerical approximation of the degenerate advection-diffusion equation, which is formally parabolic but may exhibit hyperbolic behavior. We develop both explicit and implicit finite volume weighted essentially non-oscillatory (WENO) schemes in multiple space dimensions on non-uniform computational meshes. The diffusion degeneracy is reformulated through the use of the Kirchhoff transformation. Space is discretized using WENO reconstructions with adaptive order (WENO-AO), which have several advantages, including the avoidance of negative linear weights and the ability to handle irregular computational meshes. A special two-stage WENO reconstruction procedure is developed to handle degenerate diffusion. Element averages of the solution are first reconstructed to give point values of the solution, and these point values are in turn used to reconstruct the Kirchhoff transform variable of the diffusive flux. Time is discretized using the method of lines and a Runge-Kutta time integrator. We use Strong Stability Preserving (SSP) Runge-Kutta methods for the explicit schemes, which have a severe parabolically scaled time step restriction to maintain stability. We also develop implicit Runge-Kutta methods. SSP methods are only conditionally stable, so we discuss the use of L-stable Runge-Kutta methods. We present in detail schemes that are third order in both space and time in one and two space dimensions using non-uniform meshes of intervals or quadrilaterals. Efficient implementation is described for computational meshes that are logically rectangular. Through a von Neumann (or Fourier mode) stability analysis, we show that smooth solutions to the linear problem are unconditionally L-stable on uniform computational meshes when using an implicit Radau IIA Runge-Kutta method. Computational results show the ability of the schemes to accurately approximate challenging test problems.

Keywords: hyperbolic, parabolic, degenerate diffusion, WENO reconstruction, WENO-AO, implicit L-Stable time-stepping
2000 MSC: 65M08, 65M20, 65M12, 76M12

1. Introduction

We develop both explicit and implicit finite volume weighted essentially non-oscillatory (WENO) approximations in d space dimensions of the parabolic advection-diffusion equation

$$u_t + \nabla \cdot (F(u) - D(u)\nabla u) = 0, \qquad x \in \mathbb{R}^d,\ t > 0, \tag{1}$$

$$u(x, 0) = u^0(x), \quad x \in \mathbb{R}, \tag{2}$$

with the possibly nonlinear flux $F(u) = F(u; x)$ and diffusion coefficient $D(u) = D(u; x) \geq 0$. Numerical approximation of the diffusive flux, $-D(u)\nabla u$, can be problematic when $D(u)$ is degenerate. In regions where D vanishes, the

Email addresses: arbogast@ices.utexas.edu (Todd Arbogast), huangcs@math.nsysu.edu.tw (Chieh-Sen Huang), xzhao@math.utexas.edu (Xikai Zhao)

equation exhibits hyperbolic behavior. Near a degeneracy (i.e., near where D transitions from zero to positive), the differential equation balances small and zero $D(u)$ versus the gradient of u, which may blow up.

The Kirchhof transformation is often used to mitigate the problem [1, 2]. The Kirchhoff transformation of $D(u)$ is

$$b(u; x) = \int_0^u D(v; x)\, dv. \tag{3}$$

Its gradient is then

$$\nabla b(u; x) = \nabla_x b + D(u; x)\nabla u, \tag{4}$$

where ∇_x represents partial differentiation with respect to the components of x. We recast (1) as

$$u_t + \nabla \cdot (f(u) - \nabla b(u)) = 0, \tag{5}$$

where

$$f(u; x) = F(u) + \nabla_x b. \tag{6}$$

There are many numerical schemes designed for (1)–(2). However, there are few works that specifically exploit WENO reconstructions. Explicit, finite difference WENO schemes were first developed for the problem by Liu, Shu, and Zhang [2] in 2011 (a similar scheme appears in [3]). It requires uniform computational meshes. An explicit finite volume method followed shortly afterwards in 2012, due to Bessemoulin-Chatard and Filbet [4]. Their scheme required that the equation has a special structure, and it is only second order accurate. It is not apparent that implicit WENO schemes have been developed. We present here both explicit and implicit finite volume WENO schemes of third order formal accuracy in space and time. The schemes will be developed in one and two space dimensions, on irregular computational meshes. It should be clear how to generalize our techniques to higher order schemes and $d > 2$ space dimensions.

Recent developments in WENO reconstruction technology will be used to enable us to handle (1)–(2) in a wider array of circumstances. In 2000, Levy et al. in [5] introduced a compact CWENO3 reconstruction, where they combined quadratic polynomials with linear polynomials. In 2016, Balsara et al. generalized the idea of combining low order polynomials with high order polynomials to define WENO reconstructions with adaptive order (WENO-AO) [6, 7, 8]. We use such reconstructions, since they use arbitrary linear weights, so negative weights can be avoided, and they have the flexibility to handle non-uniform computational meshes and multiple dimensions.

In [2], a double sliding average technique is developed to design a finite difference scheme for degenerate diffusion. This restricts the scheme to uniform computational meshes. In some sense, we generalize the ideas in [2] to the finite volume context and non-uniform meshes. We develop a special two-stage reconstruction procedure to handle approximation of (possibly degenerate) diffusion. In the first stage, we use WENO-AO to reconstruct the solution from its element averages $\bar{u}$. This reconstruction gives point values of the solution u. In the second stage, we evaluate point values for the Kirchhoff variable $b(u)$, and reconstruct them into a stencil polynomial. We do this for several stencils, and we combine them using smoothness indicators as in the WENO methodology.

Explicit time stepping will require the usual parabolic time step restriction that $\Delta t = O(h^2)$, where Δt is the time step and h is the minimal computational mesh element diameter. We use an explicit Strong Stability Preserving (SSP) Runge-Kutta method [9, 10, 11]. To maintain the accuracy of $O(h^3)$, we require only a second order method in time, since $\Delta t^2 = O(h^4)$ is sufficiently accurate, although we sometimes use the more popular third order SSP method. While explicit methods are interesting from a theoretical point of view, they are severely limited in application due to the extremely small time steps required.

Implicit time stepping allows one to take $\Delta t = O(h)$, and we would like to take Δt longer than the CFL limit. If one is satisfied with the CFL limit, an implicit SSP method can be used [11, 12, 13], but the time step restriction is comparable to the CFL condition of explicit methods. Instead, we propose to use L-stable Runge-Kutta methods, which are unconditionally stable and well-suited to stiff problems such as ours. We use perhaps the simplest third order L-stable Runge-Kutta method, the Radau-IIA method [14, 15]. We will show that our overall scheme is indeed unconditionally stable for smooth solutions to the linear version of (1) on uniform meshes in one dimension. We will also see numerically that Radau IIA outperforms 2-stage implicit SSP3 when long time steps are used, presumably because the SSP method is not L-stable.

In the rest of the paper, we discuss the basics of our finite volume scheme in the next section. It requires WENO reconstructions, which are described in Section 3. We first discuss one space dimension, and give WENO-AO(3,2) reconstructions combining quadratics and linear polynomials for the advection and special WENO-AO(4,3) reconstructions for the diffusion. We then discuss two space dimensions, giving similar reconstructions on logically rectangular computational meshes of quadrilaterals. WENO-AO(3,2) combines bi-quadratic and bi-linear polynomials in an efficient manner. In Section 4, we discuss the explicit and implicit Kunge-Kutta time integrators. The stability of the overall scheme is discussed in Section 5. We give a von Neumann (or Fourier mode) stability analysis of the linear problem on a uniform computational mesh in one space dimension. Smooth solutions remain stable provided $\Delta t = O(h^2)$ for the explicit scheme and unconditionally for the implicit one. In Section 6, we give numerical results that justify the order of accuracy and stability of the schemes, show superconvergence of the diffusive approximation on uniform meshes, and demonstrate that the schemes perform well for challenging test problems. Finally, in the last section we give a summary and the conclusions of our results.

2. The basic finite volume scheme

Let $\mathcal{T}_h$ be a fixed computational mesh of polytopal elements in $\mathbb{R}^d$, where h measures the size of the elements, e.g., $h = \max_{E\in\mathcal{T}_h} \text{diam}(E)$. In finite volume schemes, one approximates the average of u over an element $E \in \mathcal{T}_h$, which we denote

$$\bar{u}_E(t) = \frac{1}{|E|}\int_E u(x,t)\,dx, \tag{7}$$

where $|E|$ is the d dimensional volume of E. Fix time levels $0 = t^0 < t^1 < t^2 < \cdots$. We seek approximations to $\bar{u}_E^n$ for each $n > 0$ and $E \in \mathcal{T}_h$, and we comit a small abuse of notation by denoting these discrete approximations by $\bar{u}_E^n$. No confusion should arise, since by the end of this section, whenever u appears with a subscript or superscript, it is a discrete approximation to the true solution u.

Averaging (5) over E, we obtain

$$\bar{u}_{E,t} + \frac{1}{|E|}\int_E \nabla\cdot(f(u) - \nabla b(u))\,dx = 0. \tag{8}$$

A numerical flux function is needed for the advective term. After applying the divergence theorem and incorporating the numerical flux, we obtain

$$\bar{u}_{E,t} + \frac{1}{|E|}\int_{\partial E} (\hat{f}_E(u) - \nabla b(u)\cdot\nu_E)\,d\sigma(x) = 0, \tag{9}$$

where ∂E is the boundary of E, ν_E is the outer unit normal vector to E, and $d\sigma(x)$ is the $d-1$ dimensional measure on ∂E. We use the Lax-Friedrichs numerical flux

$$\hat{f}_E(u^+,u^-) = \frac{1}{2}[(f(u^+) + f(u^-))\cdot\nu_E - \alpha_{\text{LF}}(u^+ - u^-)], \tag{10}$$

where u^- and u^+ are approximate values of u, which will be reconstructed from data biased to being inside and outside the element (i.e., reconstructed on E and on the neighboring element), respectively, and where $\alpha_{\text{LF}} = \max_u \left|\partial f/\partial u\right| = \max_u \left|\partial(F + \nabla_x b)/\partial u\right|$.

Evaluation of the integrals over each facet of ∂E requires a quadrature rule (except in one space dimension). Let E have L_E facets, denoted $e_1,\ldots,e_{L_E}$. On each e_j, $j = 1,\ldots,L_E$, assume that we use a quadrature rule at the points $x_{j,k}$ with corresponding weights $|e_j|\omega_{j,k}$, for an appropriate range of k, where $|e_j|$ is the $d-1$ dimensional area of e_j. To make the notation more concise, denote the discrete approximation $u^{\pm}_{j,k}(t) = u^{\pm}(x_{j,k},t) \approx u(x_{j,k},t)$ and $u_{j,k}(t) \approx u(x_{j,k},t)$, and then approximate (9) as

$$\bar{u}_{E,t} + \sum_{j=1}^{L_E}\frac{|e_j|}{|E|}\sum_k \omega_{j,k}[\hat{f}_E(u^+_{j,k},u^-_{j,k}) - \nabla b(u_{j,k})\cdot\nu_E] = 0. \tag{11}$$

This is a semidiscrete approximation of (1). It remains to discuss reconstruction of the approximate values $u^{\pm}_{j,k}(t)$ and $\nabla b(u_{j,k}) \cdot \nu_E$ from the discrete solution $\bar{u}_E(t)$ at some time t, as well as the fully discrete time evolution scheme. We present reconstructions in one and two space dimensions, and we present both explicit and implicit time stepping schemes.

3. WENO reconstructions

In this section, we discuss WENO-AO reconstructions suitable for a formally third order scheme. The procedures to follow may be employed for the fixed time t, and they give $u(x_{j,k}, t)$ explicitly if $\bar{u}_E(t)\ \forall E \in \mathcal{T}_h$, are known, and implicitly otherwise. We present WENO-AO(3,2) and WENO-AO(4,3) reconstructions. The former is for reconstruction of u in the advective flux and the latter is for reconstruction of the diffusive flux $\nabla b \cdot \nu$. Both reconstructions are third order for smooth solutions and drop to second order near discontinuities. Higher order reconstructions can be developed using similar procedures. For example, a formally fifth order scheme would use WENO-AO(5,3) and WENO-AO(6,4).

In one space dimension, one can also use classic finite volume WENO reconstructions [16, 17]. Since these are somewhat more efficient than WENO-AO reconstructions, we use them to reconstruct the advective flux in some of our numerical results. We continue to use WENO-AO for the diffusive flux, since classic WENO would require negative weights.

In the case of a uniform computational mesh in one space dimension, the diffusive flux exhibits superconvergence of one higher order. To see it, one must reconstruct the advective flux to higher order. In these cases, we use classic WENO5 for advection and WENO-AO(4,3) for diffusion, or WENO7 and WENO-AO(6,4) for higher order approximation. We do not encounter negative linear weights when using classic WENO on uniform meshes.

3.1. One space dimension

In one space dimension, $E \in \mathcal{T}_h$ is an interval and ∂E consists of two points (so $L_E = 2$ and no quadrature rule is required). Let the computational mesh be defined by the grid points $\cdots < x_{-3/2} < x_{-1/2} < x_{1/2} < x_{3/2} < \cdots$. Denote the cell centers by $x_i = (x_{i+1/2} + x_{i-1/2})/2$ and let $\Delta x_i = x_{i+1/2} - x_{i-1/2}$. Now the mesh elements $E_i = [x_{i-1/2}, x_{i+1/2}]$ are indexed by i, and we simplify (11) to

$$\bar{u}_{i,t} + \frac{1}{\Delta x_i}[(\hat{f}_E(u^+_{i+1/2}, u^-_{i+1/2}) - b_x(u_{i+1/2})) - (\hat{f}_E(u^+_{i-1/2}, u^-_{i-1/2}) - b_x(u_{i-1/2}))] = 0, \tag{12}$$

where $b_x = \frac{d}{dx} b(u(x,t), x)$.

3.1.1. WENO-AO(3,2) for the advective flux in one dimension

To reconstruct $u(x)$ for $x \in E_i$ (i.e., $u^+_{i-1/2}$ and $u^-_{i+1/2}$ needed in the advective flux terms of (12), we consider three stencils, the big centered stencil $S^3 = \{E_{i-1}, E_i, E_{i+1}\}$ and the small left and right small stencils $S^2_{\mathrm{L}} = \{E_{i-1}, E_i\}$ and $S^2_{\mathrm{R}} = \{E_i, E_{i+1}\}$, as depicted in Figure 1. Construct the quadratic polynomial $P^3(x)$ so that its averages over the elements in the stencil S^3 agree with the data $\{\bar{u}_{i-1}, \bar{u}_i, \bar{u}_{i+1}\}$. Similarly construct $P^2_{\mathrm{L}}(x)$ and $P^2_{\mathrm{R}}(x)$ for the stencils S^2_{L} and S^2_{R}. Let the index set for the small stencils be denoted by $\mathcal{I} = \{L, R\}$. The WENO-AO(3,2) reconstruction of u [5, 6, 7, 8] is given for $x \in E_i$ by

$$u(x) \approx R^{3,2}_i(x) = \frac{\tilde{\alpha}}{\alpha}\Big[P^3(x) - \sum_{k\in\mathcal{I}} \beta_k P^2_k(x)\Big] + \sum_{k\in\mathcal{I}} \tilde{\beta}_k P^2_k(x), \tag{13}$$

where the *linear weights* α and β_k are arbitrary positive numbers such that $\alpha + \beta_{\mathrm{L}} + \beta_{\mathrm{R}} = 1$ (we take $\alpha = 1/2$ and $\beta_{\mathrm{L}} = \beta_{\mathrm{R}} = 1/4$). The *nonlinear weights* $\tilde{\alpha}, \tilde{\beta}_{\mathrm{L}}$, and $\tilde{\beta}_{\mathrm{R}}$ are computed in the usual way [16], namely,

$$\hat{\alpha} = \frac{\alpha}{(\epsilon + \sigma_{P^3})^\tau}, \quad \hat{\beta}_k = \frac{\beta_k}{(\epsilon + \sigma_{P^2_k})^\tau}, \quad \tilde{\alpha} = \frac{\hat{\alpha}}{\hat{\alpha} + \sum_{\ell\in\mathcal{I}} \hat{\beta}_\ell}, \quad \tilde{\beta}_k = \frac{\hat{\beta}_k}{\hat{\alpha} + \sum_{\ell\in\mathcal{I}} \hat{\beta}_\ell}, \quad k \in \mathcal{I}, \tag{14}$$

where the constants are usually chosen as $\tau = 2$ and $\epsilon = 10^{-6}$ (but see [7, 8] for consideration of these parameters). The smoothness indicator σ_{P^r} for the polynomial P^r of degree $r-1$ is computed [16] as

$$\sigma_{P^r} = \sum_{\ell=1}^{r-1} \int_{E_i} \Delta x_i^{2\ell-1} \left(\frac{d^\ell}{dx^\ell} P^r(x) \right)^2 dx. \tag{15}$$

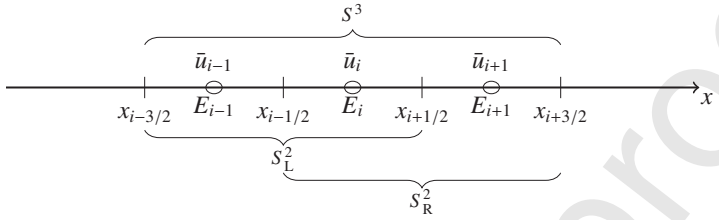

Figure 1: Stencils for WENO-AO(3,2) reconstruction.

As shown in [7, 8], when the solution u is smooth, the WENO-AO(3,2) reconstruction is third order accurate. When u has a discontinuity (and the grids remain bounded away from this discontinuity [7]), the approximation drops to second order accuracy.

3.1.2. WENO-AO(4,3) for the diffusive flux in one dimension

Because $b(u)_{xx}$ is a diffusive term, $b(u)_x$ in (12) should be reconstructed in a symmetric manner to avoid directional bias. It also needs to be approximated to third order, so $b(u)$ needs to be reconstructed to fourth order accuracy. For a third order reconstruction of the derivative at $x = x_{i+1/2}$, we use a WENO-AO(4,3) reconstruction, which uses the symmetric set of stencils shown in Figure 2.

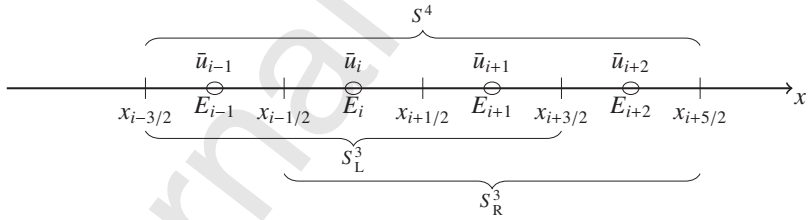

Figure 2: Stencils for WENO-AO(4,3) reconstruction.

Since our data involves local averages of u, we begin by finding a fourth order stencil polynomial P^4 over $S^4 = \{E_{i-1}, E_i, E_{i+1}, E_{i+2}\}$, and two third order stencil polynomials P^3_{L} and P^3_{R} over $S^3_{\mathrm{L}} = \{E_{i-1}, E_i, E_{i+1}\}$ and $S^3_{\mathrm{R}} = \{E_i, E_{i+1}, E_{i+2}\}$, respectively. These approximate $u(x)$.

One can imagine several ways to compute $b(u)_x$ from these three polynomial approximations of u. Perhaps the most straightforward is to define a WENO reconstruction of u, call it $R(x)$, and compute the derivative of $b(R(x))$. When u and b are smooth, one should obtain a good result. However, we are most concerned with the degenerate case where u may have a very steep gradient, so that it is nearly discontinuous. In this case, $R(x)$ smooths the steep gradient and $b(R(x))$ does not preserve the steep front. We take a different approach. We will sample point values of u from one of the three polynomials. Call a generic sample u_j and define $b_j = b(u_j)$. These values preserve the steep front, and they can be reconstructed as a polynomial for $b(u)$, which can in turn be differentiated. The three such polynomials can be combined as in the WENO-AO methodology.

Let us be more precise. As depicted in Figure 3, we first define a local computational mesh about $x_{i+1/2}$, which might as well be uniform. We suppress the index i and let $H = H_i > 0$ so that $H = O(h)$ (we take $H = (x_{i+5/2} - x_{i-3/2})/4$), and define the local points $x^j = x_{i+1/2} + jH$. The local mesh is then $\{x^{-3/2}, x^{-1/2}, x^{1/2}, x^{3/2}\}$. For the

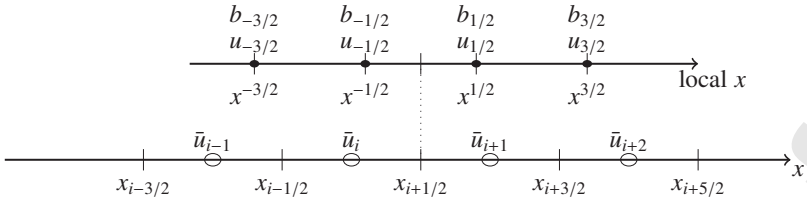

Figure 3: Reconstruction of $b(u)$ on the big stencil. The data $\bar{u}_{i-1}$, $\bar{u}_i$, $\bar{u}_{i+1}$, $\bar{u}_{i+2}$ is fit to a polynomial $P(x)$, which is evaluated at the uniformly distributed local points x^j to define $u^j = P(x^j)$, $j = -3/2, -1/2, 1/2, 3/2$. Then $b_j = b(u_j)$ are point values of b, which are fit to a polynomial $Q(x)$.

polynomial P^4 approximating u, let $u_j = P^4(x^j)$ and $b_j = b(u_j)$, $j = -3/2, -1/2, 1/2, 3/2$. Let Q^4 be the cubic polynomial interpolating the four values $b_{-3/2}$, $b_{-1/2}$, $b_{1/2}$, and $b_{3/2}$. Similarly define the quadratic polynomials $Q^3_{\rm L}$ interpolating $b(P^3_{\rm L}(x^j))$, $j = -3/2, -1/2, 1/2$, and $Q^3_{\rm R}$ interpolating $b(P^3_{\rm R}(x^j))$, $j = -1/2, 1/2, 3/2$. The WENO-AO(4,3) reconstruction of the derivative, for $x \in E_i \cup E_{i+1}$, is

$$b_x(u) \approx R^{4,3}_{x,i}(x) = \frac{\tilde{\alpha}}{\alpha}\Big[Q^{4\prime}(x) - \sum_{k\in\mathcal{I}} \beta_k Q^{3\prime}_k(x)\Big] + \sum_{k\in\mathcal{I}} \tilde{\beta}_k Q^{3\prime}_k(x), \tag{16}$$

where the linear weights $\alpha + \sum_{k\in\mathcal{I}} \beta_k = 1$.

The nonlinear weights need to be defined a bit differently from the WENO-AO(3,2) case (i.e., different from (14)). The smoothness indicators can be defined by the polynomials used for reconstruction of u or b (i.e., P or Q). The computational results suggest using P from the base data $\bar{u}$ is a bit better. We use a smoothness indicator that integrates over an interval with $x_{i+1/2}$ in its interior. Moreover, we are approximating b_x, so we should not consider first derivatives of P, or, equivalently, we consider the smoothness of hP', where h is the length of the integration interval. Perhaps the simplest such smoothness indicator is

$$\begin{aligned}\sigma_{h(P^r)'} &= \sum_{\ell=2}^{r-1} \int_{E_i\cup E_{i+1}} (\Delta x_i + \Delta x_{i+1})^{2\ell-1} \Big(\frac{d^\ell}{dx^\ell} P^r(x)\Big)^2 dx \\ &= \sum_{\ell=1}^{r-2} \int_{E_i\cup E_{i+1}} (\Delta x_i + \Delta x_{i+1})^{2\ell+1} \Big(\frac{d^{\ell+1}}{dx^{\ell+1}} P^r(x)\Big)^2 dx.\end{aligned} \tag{17}$$

The derivative is then approximated to third order when u is smooth on S^4. Otherwise, the derivative approximation drops to second order accuracy when the solution is smooth on one of the smaller stencils (and the discontinuity stays bounded away from the grid points). As is usual in WENO methods, it is not so clear what happens when the discontinuity is within $E_{i-1} \cup E_i$, i.e., no more than an element away from x_i (nevertheless, we will see good numerical results later).

3.2. Two space dimensions

WENO reconstructions on unstructured two dimensional meshes are developed in [18, 19, 20], and on three dimensional tetrahedral meshes in [21, 22]. Any of these reconstructions could be used here; however, we choose to develop a reconstruction tailored to logically rectangular meshes of quadrilaterals or cuboidal hexahedra [23]. That is, the mesh is a distortion of a rectangular mesh, and so the index space may be taken to be rectangular.

For simplicity, we only describe the reconstruction procedure in two dimensions. Extension to three (and higher) dimensions is straightforward. Given an element E_{ij}, let (x_{ij}, y_{ij}) be its centroid. For numerical stability, we define $H = \sqrt{|E_{ij}|}$ and work in the variables $\xi = (x - x_{ij})/H$ and $\eta = (y - y_{ij})/H$.

3.2.1. WENO-AO(3,2) for the advective flux in two dimensions

To compute $u^\pm$ at quadrature points in the advective part of (11), we use a WENO-AO(3,2) reconstruction to combine polynomials that approximate to order three and two (i.e., bi-quadratics and bi-linears). As shown in Figure 4,

consider four small stencils S_k^2, $k \in \mathcal{I} = \{\text{SE, SW, NE, NW}\}$, where

$$S^2_{\text{NW}} = \{E_{ij}, E_{(i-1)j}, E_{(i-1)(j+1)}, E_{i(j+1)}\}, \quad S^2_{\text{NE}} = \{E_{ij}, E_{(i+1)j}, E_{i(j+1)}, E_{(i+1)(j+1)}\},$$
$$S^2_{\text{SW}} = \{E_{ij}, E_{(i-1)j}, E_{(i-1)(j-1)}, E_{i(j-1)}\}, \quad S^2_{\text{SE}} = \{E_{ij}, E_{(i+1)j}, E_{i(j-1)}, E_{(i+1)(j-1)}\}.$$

The big stencil is $S^3 = \cup_{k\in\mathcal{I}} S_k^2$.

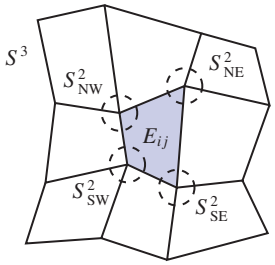

Figure 4: The five stencils used for logically rectangular WENO-AO(3,2) reconstruction on E_{ij} in two space dimensions.

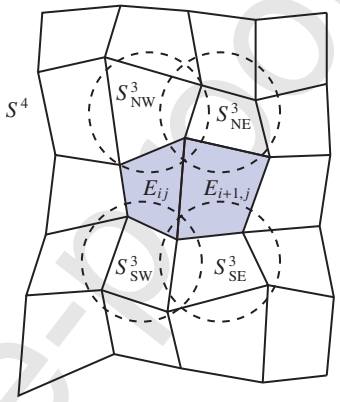

Figure 5: The five stencils used for logically rectangular WENO-AO(4,3) reconstruction of the diffusive flux on the interface between E_{ij} and $E_{i+1,j}$ in two space dimensions.

We construct the bi-linear stencil polynomials P_k^2 over S_k^2 (i.e., on the locally transformed stencil $\hat{S}_k^2$),

$$P_k^2(x,y) = b_0^k + b_1^k\xi + b_2^k\eta + b_3^k\xi\eta, \quad k \in \mathcal{I},$$

and the bi-quadratic stencil polynomial P^3 over S^3 (i.e., $\hat{S}^3$),

$$P^3(x,y) = a_0 + a_1\xi + a_2\eta + a_3\xi\eta + a_4\xi^2 + a_5\eta^2 + a_6\xi^2\eta + a_7\xi\eta^2 + a_8\xi^2\eta^2,$$

by requiring that each stencil polynomial has the same element average as u for all elements in the corresponding stencil. For any $(x,y) \in E_{ij}$, the third order reconstruction of u, $R_{ij}^{3,2}(x,y)$, is given by the two dimensional analogue of (13) with weights computed by (14), using the current small stencil index set $\mathcal{I}$ of four values. In two dimensions, we take $\epsilon = |E_{ij}|$, $\alpha = 1/2$, and $\alpha_j = 1/8$, for all $j \in \mathcal{I}$.

For a time dependent problem with a fixed computational mesh, a good way to implement the procedure above is to first define the base polynomials. Given a stencil S with its locally transformed stencil $\hat{S}$, denote the transformed elements as $\hat{E}_{pq} \in \hat{S}$. Let $\hat{\psi}_{pq}$ be the polynomial such that

$$\frac{1}{|\hat{E}_{p'q'}|}\int_{\hat{E}_{p'q'}} \hat{\psi}_{pq}(\xi,\eta)\, d\hat{A} = \begin{cases} 1, & p = p',\ q = q', \\ 0, & \text{otherwise}, \end{cases} \qquad \forall \hat{E}_{p'q'} \in \hat{S}.$$

Note that each $\hat{\psi}_{pq}(\xi,\eta)$ can be precomputed once the mesh is given. The stencil polynomial is then

$$P(x,y) = \hat{P}(\xi,\eta) = \sum_{pq} \bar{u}_{pq}\hat{\psi}_{pq}(\xi,\eta), \quad \forall E_{pq} \in S. \tag{18}$$

The smoothness indicator [19] of the polynomial $P(x,y)$ of degree m is

$$\sigma_P = \sum_{1\le|\gamma|\le m} \int_{E_{ij}} |E_{ij}|^{|\gamma|-1} (\mathcal{D}^\gamma P(x,y))^2 dA, \tag{19}$$

where $\gamma = (\gamma_1, \gamma_2)$ is a multi-index, $|\gamma| = \gamma_1 + \gamma_2$, and $\mathcal{D}$ is the derivative operator (so $\mathcal{D}^\gamma = d^{|\gamma|}/dx_1^{\gamma_1} dx_2^{\gamma_2}$). The smoothness indicators can be computed using the base polynomials (see [24]). For the polynomial P in (18),

$$\begin{aligned}
\sigma_P &= \sum_{1\le|\gamma|\le m} |E_{ij}|^{|\gamma|-1} \int_{E_{ij}} (\mathcal{D}^\gamma P(x,y))^2 dA \\
&= \sum_{1\le|\gamma|\le m} \int_{\hat{E}_{ij}} (\mathcal{D}^\gamma \hat{P}(\xi,\eta))^2 d\hat{A} \\
&= \sum_{1\le|\gamma|\le m} \int_{\hat{E}_{ij}} \Big(\sum_{pq} \bar{u}_{pq} \mathcal{D}^\gamma \hat{\psi}_{pq}(\xi,\eta) \Big)^2 d\hat{A} \\
&= \sum_{pq} \sum_{p'q'} \bar{u}_{pq}\, \bar{u}_{p'q'} \sum_{1\le|\gamma|\le m} \int_{\hat{E}_{ij}} \mathcal{D}^\gamma \hat{\psi}_{pq}(\xi,\eta) \mathcal{D}^\gamma \hat{\psi}_{p'q'}(\xi,\eta)\, d\hat{A} \\
&= \sum_{pq} \sum_{p'q'} \bar{u}_{pq}\, \bar{u}_{p'q'}\, \sigma_{ij,pq}^{p'q'},
\end{aligned} \tag{20}$$

where $\sigma_{ij,pq}^{p'q'}$ can be precomputed from the computational mesh.

3.2.2. WENO-AO(4,3) for the diffusive flux in two dimensions

Evaluation of normal derivatives in (11) requires a different reconstruction. To maintain a formal symmetry, we use the stencils depicted in Figure 5 to reconstruct a value on the facet between E_{ij} and $E_{i+1,j}$ (a similar construction is used for a facet between E_{ij} and $E_{i,j+1}$). The big stencil of 20 elements is $S^4 = \{E_{pq} : i-1 \le p \le i+2,\ j-2 \le q \le j+2\}$ and the small stencils are

$$\begin{aligned}
S^3_{\mathrm{NW}} &= \{E_{pq} : i-1 \le p \le i+1,\ j \le q \le j+2\} \quad S^3_{\mathrm{NE}} = \{E_{pq} : i \le p \le i+2,\ j \le q \le j+2\}, \\
S^3_{\mathrm{SW}} &= \{E_{pq} : i-1 \le p \le i+1,\ j-2 \le q \le j\}, \quad S^3_{\mathrm{SE}} = \{E_{pq} : i \le p \le i+2,\ j-2 \le q \le j\},
\end{aligned}$$

The bi-quadratic polynomials P^3_k, $k \in \mathcal{I} = \{\mathrm{SE}, \mathrm{SW}, \mathrm{NE}, \mathrm{NW}\}$ are constructed by matching the average of u over each element in the corresponding small stencil, and P^4 is constructed similarly over the big stencil S^4, where now P^4 is a tensor product polynomial that is fourth order in ξ and fifth order in η.

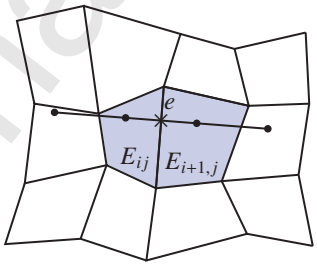

Figure 6: The sampling line and sample points used for logically rectangular WENO-AO(4,3) reconstruction of the diffusive flux. For the quadrature point, shown as a cross (×), on the interface e between E_{ij} and $E_{i+1,j}$, the sampling line goes through this point and is perpendicular to e. Sample points, shown as dots, are taken on this line. In any dimension (two space dimensions are depicted), the local computational mesh is one dimensional.

As in the one dimensional case, we sample values of u from these polynomials on a set of appropriate points. Continuing the discussion for the facet $e = E_{ij} \cap E_{i+1,j}$, let (x, y) be a quadrature point on e used in the diffusive part of (11). As depicted in Figure 6, take the line normal to the facet (i.e., in the direction of $\nu_{E_{ij}}$) and passing through (x, y), and select four sampling points on this line. Again, we should take equally spaced points, with spacing $H = O(h)$, and (x, y) should be midway between the center two points. Let these points be (x_ℓ, y_ℓ) for $\ell = 1, 2, 3, 4$. For the big stencil, we sample $u_\ell = P^4(x_\ell, y_\ell)$, compute $b_\ell = b(u_\ell)$, and reconstruct the cubic polynomial $Q^4(z)$ in one dimension interpolating b_ℓ, $\ell = 1, 2, 3, 4$, where z is the local variable on the sampling line in the direction of $\nu_{E_{ij}}$) such that $z = 0$ corresponds to the quadrature point (x, y). The derivative $Q^{4\prime}(0)$ is an approximation to $\nabla b(u) \cdot \nu_{E_{ij}}$ at (x, y).

Each small stencil $k \in \mathcal{I}$ is handled in a similar way, but we interpolate $b(P_k^3(x_\ell, y_\ell))$ at only 3 values of ℓ to define the quadratic polynomial $Q_k^3(z)$. For a "vertically" oriented interface like e, we use the three points farthest to the west (W) for the NW and SW stencils, and the three points farthest to the east (E) for the NE and SE stencils.

The reconstruction of $\nabla b(u) \cdot \nu_{E_{ij}}$ at the quadrature point (x, y) is then given by $R^{4,3}_{\nu,E_{ij}}(z)|_{z=0}$ satisfying an analogue of (16) along the sampling line, using the current small stencil index set $\mathcal{I}$ of four values. The nonlinear weighting is similar to (14). The smoothness indicators are computed from an analogue of (19) (or (20)) for the derivative, similar to (17), which is

$$\sigma_{hP'} = \sum_{2\le|\gamma|\le m} \int_{E_{ij}\cup E_{i+1,j}} |E_{ij} \cup E_{i+1,j}|^{|\gamma|-1} (\mathcal{D}^\gamma P(x, y))^2 dA. \tag{21}$$

3.3. Computing the derivative of the reconstruction

An implicit time stepping approximation of (11) will use implicit reconstructions. A nonlinear system solution procedure such as Newton's method will require evaluation of the Jacobian matrix, which will require that each implicit reconstruction, at some time level t, will need to be differentiated with respect to the unknowns $\bar{u}_E(t)$ for $E \in \mathcal{T}_h$. This is perhaps the most complicated derivative needed, so we discuss its implementation here. Fortunately, this derivative is not problem dependent, and so can be coded once for all.

We consider only the derivatives of $R_{ij}^{3,2}(x, y)$ appearing in the two dimensional analogue of (13). The derivatives of other reconstructions are computed similarly. The derivative of (13) is

$$\frac{\partial R_{ij}^{3,2}}{\partial \bar{u}_{pq}} = \frac{P^3}{\alpha}\frac{\partial \tilde{\alpha}}{\partial \bar{u}_{pq}} + \frac{\tilde{\alpha}}{\alpha}\frac{\partial P^3}{\partial \bar{u}_{pq}} + \sum_{k\in\mathcal{I}} \left[P_k^2 \Big(\frac{\partial \tilde{\beta}_k}{\partial \bar{u}_{pq}} - \frac{\beta_k}{\alpha}\frac{\partial \tilde{\alpha}}{\partial \bar{u}_{pq}} \Big) + \Big(\tilde{\beta}_k - \frac{\tilde{\alpha}\beta_k}{\alpha} \Big) \frac{\partial P_k^2}{\partial \bar{u}_{pq}} \right], \tag{22}$$

so we only need to compute the derivatives of the polynomials and the nonlinear weights. Clearly, if $E_{pq} \notin S^3$, the derivative is zero, so suppose that $E_{pq} \in S^3$. The derivative of a stencil polynomial P, written in the local basis as in (18) is

$$\frac{\partial P(x, y)}{\partial \bar{u}_{pq}} = \hat{\psi}_{pq}(\xi, \eta). \tag{23}$$

The derivatives of $\tilde{\alpha}$ and $\tilde{\beta}_k$, $k \in \mathcal{I}$ are

$$\begin{aligned}
\frac{\partial \tilde{\alpha}}{\partial \bar{u}_{pq}} &= \frac{1}{(\hat{\alpha} + \sum_{\ell\in\mathcal{I}} \hat{\beta}_\ell)^2} \Big[\frac{\partial \hat{\alpha}}{\partial \bar{u}_{pq}} \sum_{\ell\in\mathcal{I}} \hat{\beta}_\ell - \hat{\alpha} \sum_{\ell\in\mathcal{I}} \frac{\partial \hat{\beta}_\ell}{\partial \bar{u}_{pq}} \Big], \\
\frac{\partial \tilde{\beta}_k}{\partial \bar{u}_{pq}} &= \frac{1}{(\hat{\alpha} + \sum_{\ell\in\mathcal{I}} \hat{\beta}_\ell)^2} \Big[\frac{\partial \hat{\beta}_k}{\partial \bar{u}_{pq}} \Big(\hat{\alpha} + \sum_{\ell\in\mathcal{I}} \hat{\beta}_\ell \Big) - \hat{\beta}_k \Big(\frac{\partial \hat{\alpha}}{\partial \bar{u}_{pq}} + \sum_{\ell\in\mathcal{I}} \frac{\partial \hat{\beta}_\ell}{\partial \bar{u}_{pq}} \Big) \Big], \quad k \in \mathcal{I}.
\end{aligned} \tag{24}$$

where

$$\frac{\partial \hat{\alpha}}{\partial \bar{u}_{pq}} = \frac{-\tau\alpha}{(\epsilon + \sigma_{P^4})^{\tau+1}} \frac{\partial \sigma_{P^4}}{\partial \bar{u}_{pq}}, \quad \frac{\partial \hat{\beta}_k}{\partial \bar{u}_{pq}} = \frac{-\tau\beta_k}{(\epsilon + \sigma_{P_k^3})^{\tau+1}} \frac{\partial \sigma_{P_k^3}}{\partial \bar{u}_{pq}}, \quad k \in \mathcal{I}. \tag{25}$$

Finally, the derivative of the smoothness indicator for a stencil polynomial P, written in the form (20), is simply

$$\frac{\partial \sigma_P}{\partial \bar{u}_{pq}} = 2 \sum_{p'q'} \bar{u}_{p'q'} \sum_{1\le|\gamma|\le m} \int_{\hat{E}_{ij}} D^\gamma \hat{\psi}_{pq}(\xi, \eta) D^\gamma \hat{\psi}_{p'q'}(\xi, \eta)\, d\hat{A} = 2 \sum_{p'q'} \bar{u}_{p'q'} \sigma_{ij,pq}^{p'q'}. \tag{26}$$

This completes the description of the computation of the derivative of the reconstruction $R_{ij}^{3,2}$ with respect to its unknown $\bar{u}_{pq}$.

4. Time evolution

In this section, we discuss evolution of (11) in time. As is usual, we use the method of lines and a Runge-Kutta time integrator. An s stage Runge-Kutta method can be described by its Butcher Tableau (as in Table 1), consisting of the $s \times s$ matrix $A = (a_{ij})$ and s vectors c and b satisfying $\sum_j a_{ij} = c_i$ for all i and $\sum_i b_i = 1$.

c	A
	b^T

Table 1: The Butcher Tableau of a Runge-Kutta method.

0	0	0
1	1	0
	1/2	1/2

0	0	0	0
1	1	0	0
1/2	1/4	1/4	0
	1/6	1/6	2/3

Table 2: The second and third order explicit SSP Runge-Kutta methods.

1/3	5/12	−1/12
1	3/4	1/4
	3/4	1/4

Table 3: The third order implicit Radau-IIA Runge-Kutta method.

We apply the method to the initial value problem (11), but to simplify the ideas, we rewrite it as

$$\bar{u}_{E,t}(t) = \mathcal{F}(t, \bar{u}(t)), \tag{27}$$

where $\mathcal{F}$ is an operator of the cell averages $\bar{u}_{E'}$ for a subset of $E' \in \mathcal{T}_h$. This operator involves space derivatives, which are computed using the WENO reconstructions explained in the previous section. Recall that we fixed the time levels $0 = t^0 < t^1 < t^2 < \cdots$. Let $\Delta t^n = t^{n+1} - t^n$. The Runge-Kutta method is then to compute the intermediate solutions

$$\tilde{\bar{u}}_E^{n+c_i} = \bar{u}_E^n + \Delta t^n \sum_{j=1}^{s} a_{ij} \mathcal{F}(t^n + c_j \Delta t^n, \tilde{\bar{u}}^{n+c_j}), \quad i = 1, \ldots, s, \tag{28}$$

and then set

$$\bar{u}_E^{n+1} = \bar{u}_E^n + \Delta t^n \sum_{j=1}^{s} b_j \mathcal{F}(t^n + c_i \Delta t^n, \tilde{\bar{u}}^{n+c_i}). \tag{29}$$

4.1. Explicit time stepping

We need to choose a Runge-Kutta method that maintains accuracy, which in our case is third order in h. One would also like to use a Strong Stability Preserving (SSP) Runge-Kutta method, since it maintains the stability of forward Euler [9, 10, 11]. The diffusive terms will force us to take $\Delta t^n = O(h^2)$ to maintain stability, so a relatively low order method can be used.

The explicit trapezoidal or improved Euler Runge-Kutta method of Table 2 is second order in the time step, and so would be accurate to $O(h^4)$. It is also an SSP method. However, we sometimes use the more popular third order SSP method given in Table 2, since this method would work when $D \equiv 0$ and $\Delta t^n = O(h)$.

4.2. Implicit time stepping

There are no unconditionally stable SSP Runge-Kutta methods of order higher than one [11, 12, 13]. The time step restriction is comparable to the CFL condition of explicit methods. This makes them unsuitable for the advection-diffusion problem (1) that we consider.

An A-stable Runge-Kutta method is stable for the test equation $u' = au$, where $\text{Real}(a) < 0$. That is, $u^{n+1} = Q(\Delta t)u_n$ and $|Q(\Delta t)| \leq 1$. However, when the differential equation is stiff, as in a diffusion problem, it is possible that Δt is relatively large for the stiff components. An L-stable Runge-Kutta method is A-stable and satisfies $\lim_{\Delta t \to \infty} |Q(\Delta t)| = 0$. For such a method, the stiff components contribute little when the time step is large, as they should. We therefore choose to use an L-stable Runge-Kutta method. Perhaps the simplest third order L-stable Runge-Kutta method is the Radau-IIA method [14, 15], given in Table 3.

5. Stability

We can assess the stability properties of the schemes through a von Neumann (or Fourier mode) stability analysis [25, 26]. To apply this analysis, we must restrict to the linear problem on a uniform rectangular mesh. We will only consider the case of one space dimension, although the two dimensional case would be similar.

Consider the constant coefficient, linear advection-diffusion-reaction equation

$$u_t + au_x - Du_{xx} = 0, \quad x \in \mathbb{R}, \ t > 0, \tag{30}$$

where $a > 0$ and $D \geq 0$. In this case, the Lax-Friedrichs flux (10) reduces to the upwind flux, so for element E_j,

$$\hat{f}(u^+_{j+1/2}(t), u^-_{j+1/2}(t)) = a u^-_{j+1/2}(t) = a R^{3,2}_j(x_{j+1/2}, t),$$

where the reconstruction $R^{3,2}_{j-1}$ is defined in (13). We assume that the true solution u is smooth, which holds by the Cauchy-Kowalevski theorem [27] provided that the initial condition is an analytic function. In this case, the WENO methodology implies that all the nonlinear weights are approximately equal to the linear weights [24, 8, 7]. As a consequence, $R^{3,2}_j$ evaluates to the quadratic polynomial and $R^{4,3}_j$ evaluates to the cubic polynomial. Since the mesh is uniform, $\Delta x_j = h$, for all j, and the scheme (12) applied to (30) reduces to

$$\begin{aligned}\bar{u}_{j,t} &= -\frac{a}{h}[P^3_j(x_{j+1/2}, t) - P^3_{j-1}(x_{j-1/2}, t)] + \frac{D}{h^2}[hQ^{4\prime}_j(x_{j+1/2}, t) - hQ^{4\prime}_{j-1}(x_{j-1/2}, t)] \\ &= \mathcal{L}_j(\bar{u}(t)) = \frac{1}{\Delta t^n}[\lambda \mathcal{A}_j(\bar{u}(t)) + \mu \mathcal{D}_j(\bar{u}(t))], \end{aligned} \tag{31}$$

where $\lambda = a\Delta t^n/h$ and $\mu = D\Delta t^n/h^2$, and the linear operator $\mathcal{L}_j(\bar{u}(t)) = (\lambda \mathcal{A}_j(\bar{u}(t)) + \mu \mathcal{D}_j(\bar{u}(t)))/\Delta t^n$ has an advective and diffusive part.

Consider the kth single Fourier mode $\bar{u}(x,t) = T(t)\, e^{ikx}$, where in this section i is the canonical imaginary root of -1. Without loss of generality, assume $x_0 = -h/2$, so $x_{j+1/2} = jh$. Then

$$\bar{u}_{j+1/2}(t) = T(t)\, e^{ikx_{j+1/2}} = T(t)\, e^{ikjh} = T(t)\, e^{ij\theta}, \tag{32}$$

where $\theta = kh$. For an explicit scheme, we want to show A-stability, which is $|T^{n+1}| \leq |T^n|$. For an implicit scheme, we want to show also L-stability, which adds the condition $T^{n+1} \to 0$ as $\Delta t^n \to \infty$.

Substituting (32) into $\mathcal{L}$, one obtains

$$\Delta t^n \mathcal{L}_j(\bar{u}(t)) = \Delta t^n\, T(t)\, e^{ij\theta} \mathcal{L}(\theta, h) = T(t)\, e^{ij\theta}[\lambda \mathcal{A}(\theta, h) + \mu \mathcal{D}(\theta, h)], \tag{33}$$

where $\mathcal{A}(\theta, h)$ and $\mathcal{D}(\theta, h)$ will be computed from the spatial discretization. The general Runge-Kutta method of Table 1, i.e., (28)–(29), then gives the equations

$$\tilde{T}^{n+c_p} = T^n + (\lambda \mathcal{A}(\theta, h) + \mu \mathcal{D}(\theta, h)) \sum_{q=1}^{s} a_{pq} \tilde{T}^{n+c_q}, \quad p = 1, \ldots, s, \tag{34}$$

$$T^{n+1} = T^n + (\lambda \mathcal{A}(\theta, h) + \mu \mathcal{D}(\theta, h)) \sum_{q=1}^{s} b_q \tilde{T}^{n+c_q}, \tag{35}$$

after canceling the common factor $e^{ij\theta}$.

To compute $\mathcal{A}(\theta, h)$, note that

$$P^3_j(x_{j+1/2}) = u^-_{j+1/2} = \frac{1}{6}(-\bar{u}_{j-1} + 5\bar{u}_j + 2\bar{u}_{j+1}),$$

and so

$$-\Delta t^n \frac{a}{h}[P^3_j(x_{j+1/2}) - P^3_{j-1}(x_{j-1/2})] = \frac{\lambda}{6}(-\bar{u}_{j-2} + 6\bar{u}_{j-1} - 3\bar{u}_j - 2\bar{u}_{j+1}) = \lambda \mathcal{A}_j(\bar{u}),$$

which leads to

$$\mathcal{A}(\theta, h) = \frac{1}{6}(-e^{-2\theta} + 6e^{-\theta} - 3 - 2e^{\theta}) = \frac{1}{3}[-(1 - \cos\theta)^2 + i(\cos\theta - 4)\sin\theta], \tag{36}$$

which has nonpositive real part for any θ. To compute $\mathcal{D}(\theta, h)$, note that $b(u) = u$, so $Q^4 = P^4$. It is not difficult to verify that

$$\begin{aligned} u_{j-1} &= \frac{1}{24}(22\bar{u}_{j-1} + 5\bar{u}_j - 4\bar{u}_{j+1} + \bar{u}_{j+2}), & u_j &= \frac{1}{24}(-\bar{u}_{j-1} + 26\bar{u}_j - \bar{u}_{j+1}), \\ u_{j+1} &= \frac{1}{24}(-\bar{u}_j + 26\bar{u}_{j+1} - \bar{u}_{j+2}), & u_{j+2} &= \frac{1}{24}(\bar{u}_{j-1} - 4\bar{u}_j + 5\bar{u}_{j+1} + 22\bar{u}_{j+2}), \end{aligned}$$

and so

$$Q_j^{4\prime}(x_{j+1/2}) = u_{x,j+1/2} = \frac{1}{24h}(u_{j-1} - 27u_j + 27u_{j+1} - u_{j+2}) = \frac{1}{12h}(\bar{u}_{j-1} - 15\bar{u}_j + 15\bar{u}_{j+1} - \bar{u}_{j+2}).$$

Now

$$\Delta t^n \frac{D}{h^2}(hQ_j^{4\prime}(x_{j+1/2}) - hQ_{j-1}^{4\ \prime}(x_{j-1/2})) = \frac{\mu}{12}(-\bar{u}_{j-2} + 16\bar{u}_{j-1} - 30\bar{u}_j + 16\bar{u}_{j+1} - \bar{u}_{j+2}) = \mu\mathcal{D}_j(\bar{u}),$$

and so

$$\mathcal{D}(\theta, h) = \frac{1}{12}(-e^{-2\theta} + 16e^{-\theta} - 30 + 16e^{\theta} - e^{2\theta}) = -\frac{1}{3}(1 - \cos\theta)(7 - \cos\theta) \tag{37}$$

is nonpositive for any θ.

5.1. Explicit schemes

Let us denote $z = \lambda\mathcal{A}(\theta, h) + \mu\mathcal{D}(\theta, h)$. It is not surprising that the second order explicit SSP Runge-Kutta method leads us from (34)–(35) to

$$T^{n+1} = (1 + z + \tfrac{1}{2}z^2)T^n, \tag{38}$$

and the stability condition is $|1 + z + \frac{1}{2}z^2| \le 1$. It is not easy to characterize when z meets this condition. Instead, we will consider the case of pure diffusion, so $\lambda = 0$ and $z = \mu\mathcal{D}(\theta, h) = -\mu(1 - \cos\theta)(7 - \cos\theta)/3$ is real and nonpositive. Then we simply need that $z \ge -2$. This must hold for all θ, so we need that

$$\max_{c\in[-1,1]} \mu(1 - c)(7 - c) \le 6 \quad \Longrightarrow \quad \mu = \frac{D\Delta t^n}{h^2} \le \frac{3}{8} = 0.375. \tag{39}$$

When there is advection, this condition is asymptotically correct as $h \to 0$.

The third order order explicit SSP Runge-Kutta method leads to

$$T^{n+1} = (1 + z + \tfrac{1}{2}z^2 + \tfrac{1}{6}z^3)T^n. \tag{40}$$

In the case of pure diffusion, i.e., z real and nonpositive, stability requires that $z \ge z_* = -2.51275$, and so

$$\max_{c\in[-1,1]} \mu(1 - c)(7 - c) \le -3z_* \quad \Longrightarrow \quad \mu = \frac{D\Delta t^n}{h^2} \le \frac{-3z_*}{16} = 0.47114. \tag{41}$$

If we use WENO-AO(6,4) to compute the diffusion terms (combined with third order SSP Runge-Kutta), we find that

$$\begin{aligned}\mathcal{D}(\theta, h) &= \frac{1}{180}(2e^{-3\theta} - 27e^{-2\theta} + 270e^{-\theta} - 490 + 270e^{\theta} - 27e^{2\theta} + 2e^{3\theta}) \\ &= -\frac{1}{45}(1 - \cos\theta)(4\cos^2\theta - 23\cos\theta + 109),\end{aligned}$$

which is again nonpositive, and

$$\mu = \frac{D\Delta t^n}{h^2} \le 0.415712. \tag{42}$$

This agrees with the value found in [2].

5.2. Implicit scheme

Again with $z = \lambda\mathcal{A}(\theta, h) + \mu\mathcal{D}(\theta, h)$, the Radau IIA Runge-Kutta method (Table 3) applied to (34)–(35) gives

$$\tilde{T}^{n+1/3} = T^n + \frac{z}{12}(5\tilde{T}^{n+1/3} - T^{n+1}), \tag{43}$$

$$T^{n+1} = \tilde{T}^{n+1} = T^n + \frac{z}{4}(3\tilde{T}^{n+1/3} + T^{n+1}). \tag{44}$$

Inverting the 2×2 system leads to

$$\tilde{T}^{n+1} = \frac{48 + 16z}{5z^2 - 29z + 48} T^n = Q(z)\, T^n. \tag{45}$$

It is apparent that if the scheme is A-stable for each Fourier mode (i.e., $|Q(z)| \leq 1$), then it will be L-stable, since as $|z| \to \infty$, $|Q(z)| \to 0$.

Let $z = \gamma + i\delta$, and recall that $\gamma \leq 0$. Then

$$\begin{aligned} |Q(z)|^2 = Q(z)Q(\bar{z}) &= \frac{(48 + 16\gamma)^2 + 256\delta^2}{(5\gamma^2 - 5\delta^2 - 29\gamma + 48)^2 + \delta^2(10\gamma - 29)^2} \\ &= \frac{(48 + 16\gamma)^2 + 256\delta^2}{(5\gamma^2 - 29\gamma + 48)^2 + 25\delta^4 - 10\delta^2(5\gamma^2 - 29\gamma + 48) + \delta^2(10\gamma - 29)^2}. \end{aligned}$$

It is not difficult to verify that

$$\begin{aligned} (48 + 16\gamma)^2 &\leq (5\gamma^2 - 29\gamma + 48)^2, \\ 256\delta^2 &\leq 25\delta^4 - 10\delta^2(5\gamma^2 - 29\gamma + 48) + \delta^2(10\gamma - 29)^2 \end{aligned}$$

when $\gamma \leq 0$ for any δ. Thus the implicit scheme is (unconditionally) A-stable, and also L-stable, for smooth solutions to the linear problem on a uniform computational mesh. We remark that the intermediate time amplification factor $\tilde{T}^{n+1/3}$ is also L-stable.

6. Numerical results

We have developed computer programs to test the algorithms described in this paper. The codes use one of the Runge Kutta time stepping methods described in Section 4, second order explicit SSP Runge-Kutta (SSP2), third order explicit SSP Runge-Kutta (SSP3), or Radau IIA Runge-Kutta (Radau3). If not stated otherwise, the advection is approximated using WENO-AO(3,2) reconstructions, as described in Sections 3.1.1 or 3.2.1, and diffusion is approximated using WENO-AO(4,3) reconstructions, as described in Sections 3.1.2 or 3.2.2. Our schemes do *not* require negative weights in the WENO reconstructions, because WENO-AO is used (or classic WENO is used on uniform meshes). We describe our schemes by specifying the time stepping, advective reconstructions, and diffusive reconstructions. For example, our main schemes are

SSP2/WENO-AO(3,2)/WENO-AO(4,3), abbreviated as explicit SSP2-3-4,

SSP3/WENO-AO(3,2)/WENO-AO(4,3), abbreviated as explicit SSP3-3-4,

Radau3/WENO-AO(3,2)/WENO-AO(4,3), abbreviated as implicit Radau3-3-4,

SSP3/WENO-AO(5,3)/WENO-AO(6,4), abbreviated as explicit SSP3-5-6.

We will use $\Delta t = O(h^2)$ for the explicit schemes and $\Delta t = O(h)$ for the implicit one. Without superconvergence effects, we would expect these schemes to converge as $O(\Delta t^2 + h^3) = O(h^3)$ for explicit SSP2-3-4, $O(\Delta t^3 + h^3) = O(h^3)$ for explicit SSP3-3-4 and implicit Radau3-3-4, and $O(\Delta t^3 + h^5) = O(h^5)$ for explicit SSP3-5-6.

We present numerical results for test problems similar to those considered by Liu, Shu, and Zhang [2] and Kurganov and Tadmor [28]. Most of our test examples use periodic boundary conditions, but a few use Dirichlet conditions. The results we present below are comparable in accuracy to those in the aforementioned papers, but our meshes are non-uniform in 1D and consist of quadrilaterals in 2D. Moreover, we include results from the implicit scheme, which uses a much longer time step.

In one space dimension, we use the symbol M to denote the number of mesh elements. Non-uniform meshes are created by randomly perturbing each interior point of a uniform mesh by $\pm 25\%$ of $h = \Delta x = L/M$, for a domain of length L. The linear weights used in the reconstructions are $\alpha = 1/2$ and $\beta_{\mathrm{L}} = \beta_{\mathrm{R}} = 1/4$. We take $\epsilon = 1E - 6$ in (14) defining the nonlinear weights.

In two space dimensions, we use a square computational domain. Our computational meshes are derived from perturbations of uniform meshes of $M \times M$ elements, and in this case we define h to be the spacing of the uniform

mesh. Each grid point (not on the boundary) is perturbed uniformly by ±25% in each coordinate direction. This results in meshes of quadrilaterals. The linear weights used in the reconstructions are $\alpha = 1/2$ and all $\beta_k = 1/8$. The nonlinear weights use a scaling as in (14), but the parameter ϵ for element $E \in \mathcal{T}_h$ is mesh weighted by factor $\epsilon = |E|$ (as suggested in [7, 8]). The spacing H of the sampling points on the sampling line needed for the reconstructions of the diffusion terms is taken to be the unperturbed mesh spacing h. Except for the convergence studies, all other two dimensional results use a computational mesh of $M = 80$ quadrilateral elements in each direction.

6.1. Convergence and stability studies

We begin with some simple tests to show the superconvergence phenomena when using uniform computational meshes, and follow with general tests on non-uniform meshes.

6.1.1. Superconvergence tests

On uniform computational meshes, we expect that the diffusive terms are approximated to $O(h^4)$ when using WENO-AO(4,3), and to $O(h^6)$ when using WENO-AO(6,4). To see this superconvergence, the advective term needs to use reconstructions at least this accurate, so we employed classic WENO5 and WENO7 for these tests. Moreover, the time error must be sufficiently accurate. For the explicit schemes, the stability results of Section 5 show that $\Delta t = O(h^2)$, and so SSP2/WENO5/WENO-AO(4,3) should be $O(h^4)$ accurate, and SSP3/WENO7/WENO-AO(6,4) should be $O(h^6)$ accurate.

We first test our schemes in the simple case of

$$u_t + a(u^2/2)_x - Du_{xx} = 0 \tag{46}$$

over $[0, 2\pi]$. With $a = 0$ and $D = 1$, we have the heat equation. If we impose the initial condition $u^0(x) = \sin x$, the exact solution is $u(x, t) = \sin x e^{-Dt}$. We can see from Table 4 that the explicit schemes show fourth and sixth order convergence of the error on a uniform computational mesh. That is, the superconvergence is seen.

Table 4: The heat equation. Error and convergence order at time $t = 1$ using $D = 1$ on a uniform mesh.

M	L_h^1 error	order	L_h^∞ error	order
SSP2/WENO5/WENO-AO(4,3) with $\Delta t = 0.35h^2$				
20	2.369E-03	4.06	5.587E-04	4.02
40	6.606E-05	5.16	1.588E-05	5.14
80	2.379E-06	4.80	5.845E-07	4.76
160	1.200E-07	4.31	2.984E-08	4.29
SSP3/WENO7/WENO-AO(6,4) with $\Delta t = 0.4h^2$				
20	2.823E-04	5.62	8.335E-05	5.53
40	4.895E-06	5.85	1.439E-06	5.86
80	9.204E-08	5.73	2.601E-08	5.79
160	1.105E-09	6.38	3.340E-10	6.28

Table 5: Burgers equation with diffusion $D = 1$. Error and convergence order at time $t = 2$ on a uniform mesh.

M	L_h^1 error	order	L_h^∞ error	order
SSP2/WENO5/WENO-AO(4,3) with $\Delta t = 0.35h^2$				
20	1.937E-03	2.76	4.949E-04	2.99
40	1.550E-04	3.64	3.921E-05	3.66
80	4.582E-06	5.08	1.167E-06	5.07
160	1.257E-07	5.19	3.320E-08	5.14
SSP3/WENO7/WENO-AO(6,4) with $\Delta t = 0.4h^2$				
20	4.988E-05	6.25	1.280E-05	6.28
40	2.708E-07	7.53	7.563E-08	7.40
80	5.035E-09	5.75	1.350E-09	5.81
160	8.425E-11	5.90	2.320E-11	5.86

We now consider $a = 1$ and $D = 1$, giving Burgers equation with diffusion. Exact solutions can be found using the Hopf-Cole transformation, and we take the exact solution

$$u(x, t) = \frac{-2D \cos x \exp(-Dt)}{2 + \sin x \exp(-Dt)}. \tag{47}$$

The results appear in Table 5, and we see superconvergence. In fact, the lower order scheme has $O(h^5)$ convergence of the advection, so those results appear somewhat better than the expected $O(h^4)$ up to $M = 160$. The convergence drops to $O(h^4)$ for larger M. The higher order scheme is indeed $O(h^6)$.

We next test superconvergence for the porous medium equation (PME), given below in Section 6.2 (i.e., (49)), for which the Barenblatt solution (50) is known. We take as initial condition the Barenblatt solution at $t = 1$. The domain is restricted to $[-6, 6]$, and we set the boundary condition $u(\pm 6, t) = 0$ for $t > 1$. Table 6 shows the convergence rate at

Table 6: Porous medium equation with $m = 8$. Error and convergence order at time $t = 1.05$ on a uniform mesh.

M	L_h^1 error	order	L_h^∞ error	$t = 1.05$ order
SSP2/WENO5/WENO-AO(4,3) with $\Delta t = 0.04375h^2$				
20	7.166E-06	8.92	3.114E-06	9.86
40	5.765E-07	3.20	4.266E-07	2.52
80	3.103E-08	4.52	2.405E-08	4.45
160	1.815E-09	4.24	1.427E-09	4.22
SSP3/WENO7/WENO-AO(6,4) with $\Delta t = 0.05h^2$				
20	1.882E-05	7.04	1.699E-05	6.04
40	7.577E-07	4.07	9.810E-07	3.62
80	1.319E-08	6.26	2.132E-08	5.92
160	1.822E-10	6.40	3.859E-10	6.00

$t = 1.05$, with $|x| \le 1.5$ (i.e., in the smooth region of the solution) and $m = 8$. We continue to see the superconvergence effect, and the results are a bit better than the third order discontinuous Galerkin scheme of Zhang and Wu [29, Table 1].

6.1.2. Convergence tests in two space dimensions

We now generalize (46) as the two-dimensional Burgers equation with diffusion,

$$u_t + a[(u^2/2)_x + (u^2/2)_y] - D(u_{xx} + u_{yy}) = 0, \tag{48}$$

on the domain $[0, 2]^2$.

Table 7: Heat Equation in 2D. Error and convergence order using $\Delta t = 0.2h^2$ (explicit SSP3-3-4) and $\Delta t = h$ (implicit Radau3-3-4) on quadrilateral meshes based on perturbation of uniform meshes.

M	L_h^1 error	order	L_h^∞ error	order
Explicit SSP3-3-4				
20	4.186E-04	3.97	3.744E-04	3.90
40	1.299E-05	5.01	1.903E-05	4.30
80	6.360E-07	4.35	1.179E-06	4.01
160	3.994E-08	3.99	7.596E-08	3.96
Implicit Radau-3-3-4				
20	1.368E-02	3.30	5.940E-03	3.47
40	2.003E-03	2.76	8.305E-04	2.84
80	2.812E-04	2.83	1.133E-04	2.87
160	3.757E-05	2.90	1.495E-05	2.92

Table 8: Burgers equation in 2D with diffusion. Error and convergence order of the implicit Radau3-3-4 scheme using $\Delta t = 5h$ at time $t = 1$ on quadrilateral meshes meshes.

M	L_h^1 error	order	L_h^∞ error	order
$D = 0.1$				
20	3.254E-03	——	1.570E-03	——
40	4.908E-04	2.73	2.172E-04	2.85
80	6.687E-05	2.88	2.910E-05	2.90
160	8.742E-06	2.94	3.764E-06	2.95
$D = 0.0001$				
20	2.023E-08	——	5.617E-08	——
40	5.705E-09	1.83	2.487E-08	1.18
80	1.058E-09	2.43	5.766E-09	2.11
160	1.330E-10	2.99	6.748-10	3.10

We first take $a = 0$, $D = 1$ (i.e., the heat equation), and the initial condition $u(x, y, 0) = \sin(\pi(x + y))$. For the explicit scheme, we used $\Delta t = 0.2h^2$ and ran the simulation to time $t = 0.02$. For the implicit scheme, we used $\Delta t = h$ and ran to time $t = 0.2$. We used meshes of $M \times M$ elements (so $h = 2/M$).

The rates of convergence appear in Table 7. The rates of convergence bounce around a bit as M increases, probably due to the use of randomly perturbed meshes of quadrilaterals. We see superconvergence of order four for the explicit scheme. The time stepping here is accurate enough, since we use the third order SSP method with $\Delta t = O(h^2)$, so the temporal error is $O(\Delta t^3) = O(h^6)$ is sixth order accurate in space. It seems that the existence of an underlying uniform mesh is enough to give superconvergence in space. In fact, we see this effect for one dimensional problems as well when we define non-uniform meshes from a uniform mesh by randomly perturbing each internal grid point by ±25%. To drop the scheme to order three, we need to use a non-uniform mesh of grid points produced in a nested fashion, namely, all coarse grid points are retained and new points are added by perturbing the midpoint of the two adjacent coarse grid points.

The implicit results show only the expected third order convergence, since now $\Delta t = O(h)$ and the time stepping, being third order, does not allow us to see the superconvergent space approximation.

Finally, we take $a = 1$ and the exact solution

$$u(x, y, t) = -2D\pi \frac{\cos(\pi(x + y)) \exp(-2D\pi^2 t)}{2 + \sin(\pi(x + y)) \exp(-2D\pi^2 t)}.$$

The rates of convergence for the implicit Radau3-3-4 scheme are given in Table 8 for a large and small diffusion coefficient D and using $\Delta t = 5h$. We see the expected third order convergence, even for the relatively long time step used.

6.1.3. Stability tests for the implicit time integrator

Since the 2-stage implicit SSP3 method is not L-stable, it is not expected to perform for relatively long time steps. In fact, it is known that implicit SSP methods lead to oscillations when the stability constraint fails to be satisfied [13]. Our implicit Radau3-3-4 scheme is unconditionally L-stable for the linear problem.

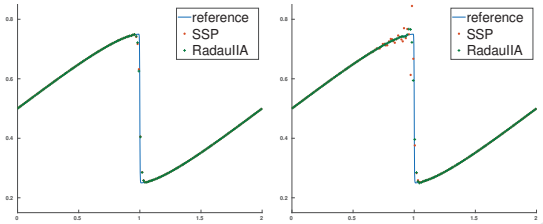

$\Delta t = 2h$ (SSP is stable)

$\Delta t = 5h$ (both unstable)

Figure 7: Burgers equation. Comparison of the implicit SSP3/WENO-AO(3,2) scheme and the implicit Radau3-3-4 scheme, using a non-uniform mesh of $M = 160$ elements.

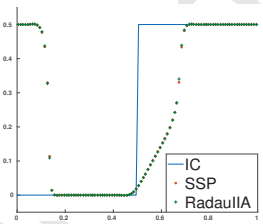

$\Delta t = 0.5h$ (SSP is stable)

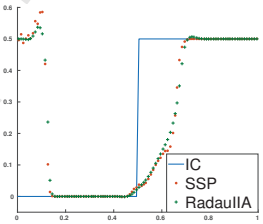

$\Delta t = 2h$ (both unstable)

Figure 8: Buckley-Leverett hproblem. Comparison of the implicit SSP3/WENO-AO(3,2) scheme and the implicit Radau3-3-4 scheme, using a non-uniform mesh of $M = 100$ elements.

We compare solutions of the implicit SSP3/WENO-AO(3,2) scheme (with no diffusion) and the implicit Radau3-3-4 scheme. In Figure 7, we show results for the nonlinear Burgers equation (47) ($a = 1$, $D = 0$) with $u(x, 0) = \frac{1}{2}(1 - \sin x)$ at time $t = 2$. We use a non-uniform mesh of $M = 160$ elements. When $\Delta t = 2h$, the SSP scheme is stable, and gives good results, but Radau does likewise. However, when $\Delta t = 5h$, both schemes go unstable (the problem is not linear and the solution is not smooth), but Radau gives better results.

In Figure 8, we show results at time $t = 0.085$ for the nonlinear Buckley-Leverett problem using the flux (55) with an initial jump discontinuity. We use a non-uniform mesh of $M = 100$ elements. When $\Delta t = 0.5h$, SSP is stable, and both schemes gives good results. When $\Delta t = 2h$, both schemes go unstable, but, again, Radau gives better results. For this example, we do *not* use the Koren limiter used in [13], so the solution is not quite as sharp as obtained in that paper.

6.2. The porous medium equation (PME)

We now show solutions for the porous medium equation (PME), i.e.,

$$u_t = (u^m)_{xx}, \tag{49}$$

in which m is a constant greater than one. The Barenblatt solution [30] of the PME is

$$B_m(x, t) = t^{-k} \left[\left(1 - \frac{k(m-1)}{2m} \frac{|x|^2}{t^{2k}} \right)_+ \right]^{1/(m-1)}, \quad m > 1, \tag{50}$$

where $u_+ = \max(u, 0)$ and $k = (m + 1)^{-1}$. This solution, for any time $t > 0$, has compact support $[-\alpha_m(t), \alpha_m(t)]$ with the interface $|x| = \alpha_m(t)$ moving outward at a finite speed, where

$$\alpha_m(t) = \sqrt{\frac{2m}{k(m-1)}} t^k.$$

6.2.1. The Barenblatt solution

For the PME (49) on $[-6, 6]$, we take as initial condition the Barenblatt solution (50) at $t = 1$, and the boundary condition $u(\pm 6, t) = 0$ for $t > 1$. We divide the computational domain into $M = 160$ cells, and randomly perturb each point uniformly by $\pm 25\%$ of $h = 12/M$. We plot the numerical solution at time $t = 2$ for $m = 2$, 4, 6, and 8 in Figure 9. The explicit SSP2-3-4=SSP2/WENO-AO(3,2)/WENO-AO(4,3) and SSP3-5-6=SSP3/WENO-AO(5,3)/WENO-AO(6,4) schemes (although there is no advection in this problem) use a time step so that

$$\max_u |b'(u)|\Delta t / \min_i h_i^2 = 0.35 \text{ or } 0.4, \text{ respectively.}$$

Both explicit schemes produce accurate numerical solutions without noticeable oscillations. The solutions for the implicit Radau3-3-4 scheme are nearly identical, and they appear in Figure 10. For these, we use only $M = 120$ and $\Delta t = h$.

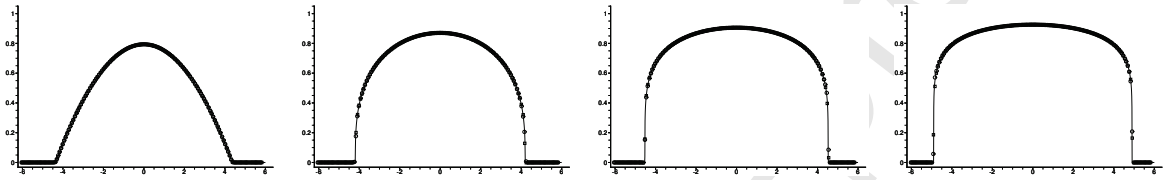

$m = 2$ $m = 4$ $m = 6$ $m = 8$

Figure 9: Barenblatt solution of the PME on a non-uniform mesh of $M = 160$ elements at time $t = 2$. Circles are for the explicit SSP2-3-4=SSP2/WENO(3,2)/WENO-AO(4,3) scheme, squares are for SSP3-5-6/WENO(5,3)/WENO-AO(6,4), using Δt satisfying $\max_u |b'(u)|\Delta t/\min_i h_i^2 = 0.35$ and $\max_u |b'(u)|\Delta t/\min_i h_i^2 = 0.4$, respectively. The solid line is the exact solution.

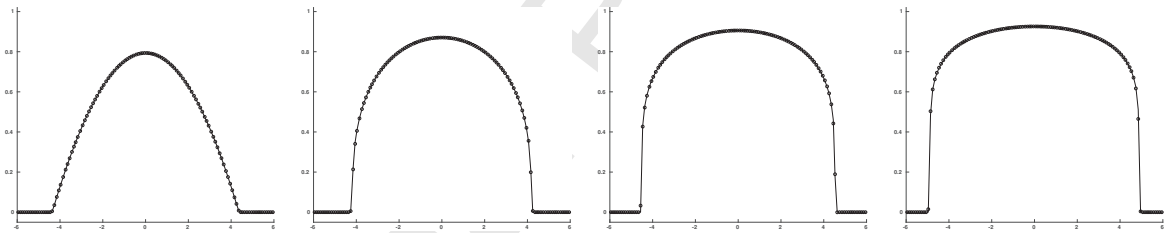

$m = 2$ $m = 4$ $m = 6$ $m = 8$

Figure 10: Barenblatt solution of the PME on a non-uniform mesh of $M = 120$ elements at time $t = 2$ using implicit Radau3-3-4 and $\Delta t = h$. The solid line is the exact solution.

6.2.2. Collision of two boxes

We also consider the solution of the PME problem representing the collision of two initial boxes with different heights. We take $m = 6$ in the PME and the initial condition

$$u(x, 0) = \begin{cases} 1, & \text{if } x \in (-4, -1), \\ 2, & \text{if } x \in (0, 3), \\ 0, & \text{otherwise.} \end{cases} \tag{51}$$

The evolution of the numerical solution on non-uniform meshes is shown in Figure 11 for the explicit scheme. The implicit scheme gives very similar results, and they are shown in Figure 12.

We now consider the collision of two boxes with different heights and an $x-$dependent diffusion term, so

$$u_t = \left((x + 6)^2 u^5 u_x\right)_x, \quad x \in [-6, 6]. \tag{52}$$

Using the Kirchhoff transformation, this becomes

$$u_t + ((x + 6)u^6/3)_x = \left((x + 6)^2 u^6/6\right)_{xx}, \quad x \in [-6, 6]. \tag{53}$$

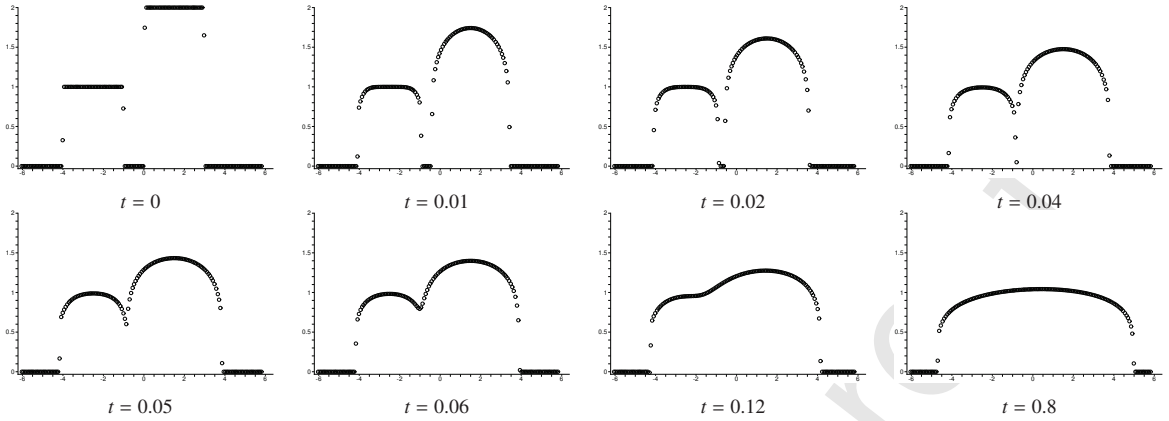

Figure 11: PME collision of two boxes with different heights for $m = 6$ on a non-uniform mesh of $M = 160$ elements for the explicit SSP2-3-4 scheme, with Δt satisfying $\max_u |b'(u)|\Delta t/\min_i h_i^2 = 0.25$.

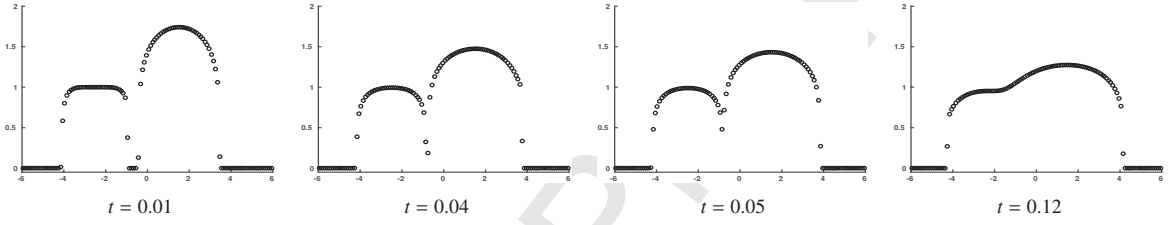

Figure 12: PME collision of two boxes with different heights for $m = 6$ on a non-uniform mesh of $M = 120$ elements for the implicit Radau3-3-4 scheme, with $\Delta t = 0.005h$ for the first 20 steps and then $\Delta t = 0.05h$.

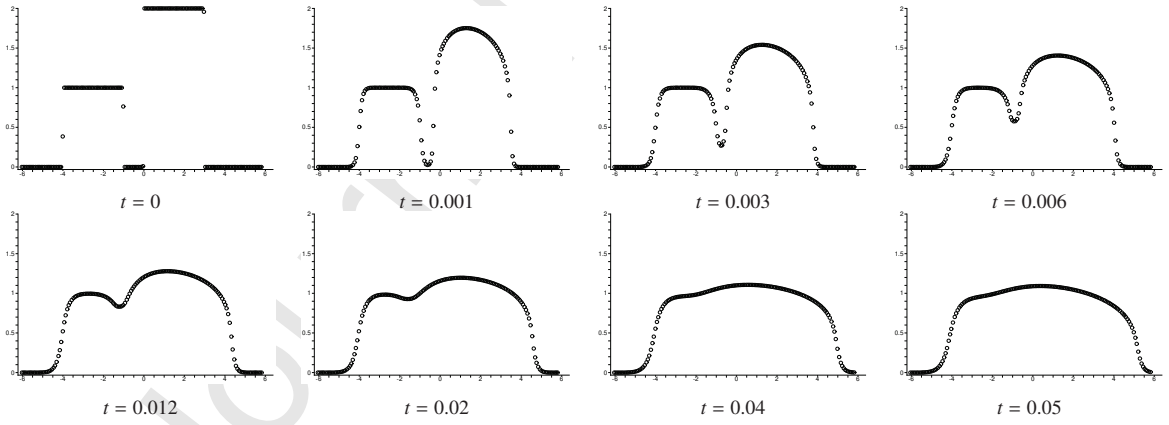

Figure 13: PME collision of two boxes with different heights for $m = 6$ using an $x-$dependent diffusion on a non-uniform mesh of $M = 160$ elements for the explicit SSP2-3-4 scheme, with Δt satisfying $\max_u |b'(u)|\Delta t/\min_i h_i^2 = 0.25$.

The numerical solution for the explicit SSP2-3-4 scheme, with initial condition (51), is shown in Figure 13. The $x-$dependent diffusion causes no difficulty.

Due to the $x-$dependence, there is more diffusion on the right side of the domain than on the left, and this can be seen in the results, although the effect is somewhat subtle to the eye. However, comparison to the original PME (49) reveals the effect. With $m = 6$, (49) is $u_t = (6u^5u_x)_x$, so the diffusion coefficient is the constant value 6, whereas (53) has coefficient $(x + 6)^2$ on the domain $[-6, 6]$, which varies from 0 to 144. However, initially $u = 0$ for $x < -4$, so the

diffusion coefficient is more like 4 to 144, i.e., it is at least about as much as in the original PME. Comparing Figure 11 (or Figure 12) to Figure 13, we see that the latter has more diffusion overall—perhaps about ten times more, given the time scales. Moreover, the edges (or steep fronts) on the right sides of the boxes are more diffused than those on the left in Figure 13 compared to the original PME results. These observations are to be expected from the nature of the $x-$dependent diffusion.

6.2.3. The PME in two dimensions

We consider now the two-dimensional porous medium equation

$$u_t = \Delta u^m \tag{54}$$

on the domain $[-10, 10]^2$, where we take $m = 2$ and $m = 8$. The initial condition is taken to represent two round bumps, and it is

$$u(x, y, 0) = \begin{cases} \exp\left(-1/[6-(x-2)^2-(y+2)^2]\right), & \text{if } (x-2)^2+(y+2)^2 < 6, \\ \exp\left(-1/[6-(x+2)^2-(y-2)^2]\right), & \text{if } (x+2)^2+(y-2)^2 < 6, \\ 0, & \text{otherwise.} \end{cases}$$

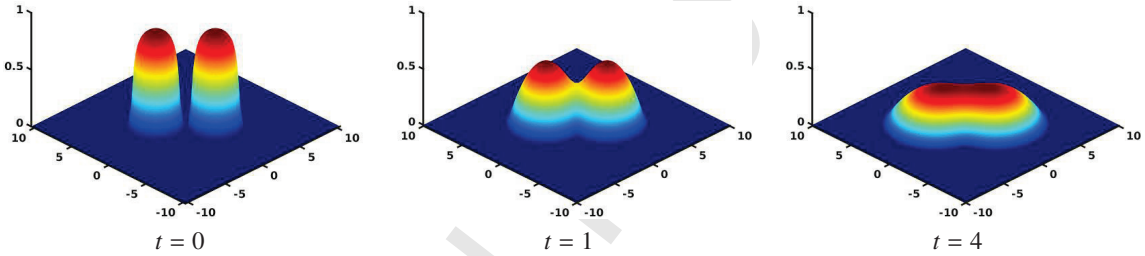

Figure 14: The solution to the 2D PME with $m = 2$. The implicit Radau3-3-4 solution using $M = 80$ quadrilateral elements and $\Delta t = h/2$.

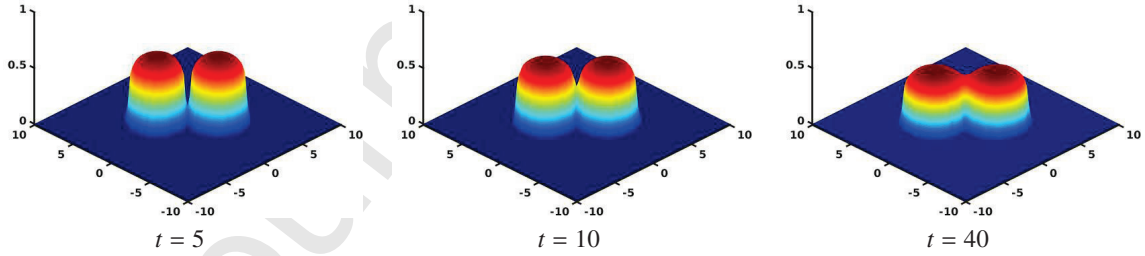

Figure 15: The solution to the 2D PME with $m = 8$. The implicit Radau3-3-4 solution using $M = 80$ quadrilateral elements and $\Delta t = 2h$.

The explicit scheme uses $\Delta t = 0.1h^2$, while the implicit scheme uses $\Delta t = 0.5h$ for $m = 2$ and $\Delta t = 2h$ for $m = 8$. The explicit and implicit schemes give nearly identical plots, so we only show the implicit results for $m = 2$ in Figure 14 at times $t = 0$, 1, and 4, and for $m = 8$ in Figure 15 at times $t = 5$, 10, and 40.

6.3. Buckley-Leverett equation

The Buckley-Leverett flux function is defined as

$$f_{\mathrm{BL}}(u) = \frac{u^2}{u^2 + (1-u)^2}, \tag{55}$$

which is a nonconvex function. It arises in problems involving flow in porous media.

6.3.1. The Buckley-Leverett equation in one dimension

We consider the scalar Buckley-Leverett equation

$$u_t + f_{\mathrm{BL}}(u)_x - D(\nu(u)u_x)_x = 0, \tag{56}$$

where we set $D = 0.01$ and

$$\nu(u) = 4u(1-u). \tag{57}$$

The initial condition is

$$u(x,0) = \begin{cases} 1-3x, & 0 \le x \le \frac{1}{3}, \\ 0, & \frac{1}{3} \le x \le 1, \end{cases} \tag{58}$$

and the boundary condition is $u(0,t) = 1$. The results given in Figure 16 show good agreement with the reference solution, for both third order explicit and implicit schemes.

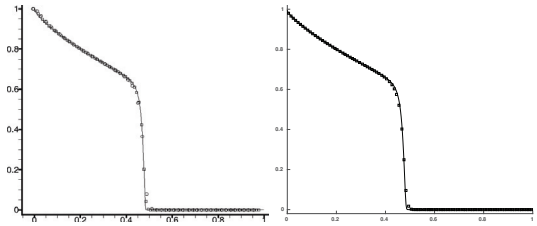

Figure 16: Solution of the Buckley-Leverett equation with initial condition (58) at time $t = 0.2$ on a non-uniform mesh. On the left are results for explicit SSP2-3-4 with Δt satisfying $\max_u |b'(u)|\Delta t/\min_i h_i^2 = 0.25$, and depicting with circles for $M = 50$ and squares for $M = 100$. On the right are results for implicit Radau3-3-4 with $\Delta t = h$. The solid lines are the reference solutions with $N = 800$ (explicit) and $M = 400$ (implicit).

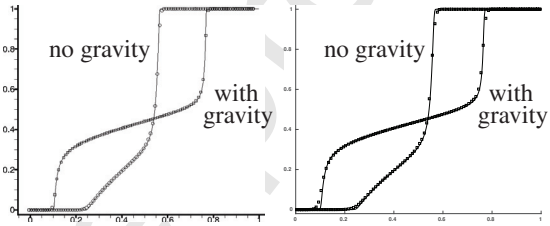

Figure 17: Solution of the Buckley-Leverett Riemann problem (59) at time $t = 0.2$ on a non-uniform mesh of $M = 100$ elements, showing both the original problem (wider front) and the one imitating gravitation (narrower front). On the left is explicit SSP2-3-4, with Δt satisfying $\max_u |b'(u)|\Delta t/\min_i h_i^2 = 0.25$. On the right is implicit Radau3-3-4 with $\Delta t = 2h$ (no gravity) and h (with gravity). Solid lines are the reference solutions using $M = 800$ (explicit) and $M = 400$ (implicit).

We also consider the problem with an initial condition representing a Riemann problem, i.e.,

$$u(x,0) = \begin{cases} 0, & 0 \le x < 1 - \frac{1}{\sqrt{2}}, \\ 1, & 1 - \frac{1}{\sqrt{2}} \le x \le 1. \end{cases} \tag{59}$$

We solve the problem as stated above, with the diffusion coefficient (57) and the flux f_{BL}. We also solve the problem with the modified flux function

$$f_{\mathrm{BLg}}(u) = f_{\mathrm{BL}}(u)(1 - 5(1-u)^2) = \frac{u^2}{u^2 + (1-u)^2}(1 - 5(1-u)^2)$$

to imitate gravitational effects. Results are shown in Figure 17, and again very good agreement with the reference solution is observed in both cases for both explicit and implicit schemes.

6.3.2. The Buckley-Leverett equation in two dimensions

The following is a modified Buckley-Leverett problem:

$$u_t + \nabla F(u) - D\Delta u = 0, \quad F(u) = \begin{pmatrix} f_{\mathrm{BL}}(u) \\ f_{\mathrm{BLg}}(u) \end{pmatrix} = \frac{u^2}{u^2 + (1-u)^2}\begin{pmatrix} 1 \\ 1 - 5(1-u)^2 \end{pmatrix}, \tag{60}$$

which more appropriately incorporates gravitational effects. We consider this problem on $[-1.5, 1.5]^2$ with (again) very small $D = 0.01$. The initial condition is

$$u(x,y,0) = \begin{cases} 1, & \text{if } x^2 + y^2 \le 0.5, \\ 0, & \text{otherwise.} \end{cases}$$

The explicit and implicit schemes use $\Delta t = 2h^2$ and $\Delta t = h$, respectively, and they give nearly identical plots. We show the implicit results in Figure 18 at time $t = 0.5$.

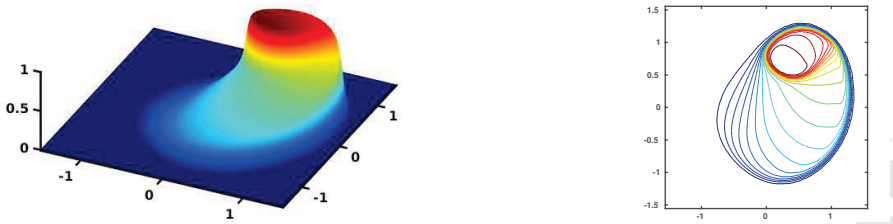

Figure 18: The 2D Buckley-Leverett equation. The implicit solution using $M = 80$ quadrilateral elements and $\Delta t = h$ at time $t = 0.5$ in profile (left) and as a contour plot (right).

6.4. A glacier growth model in one space dimension

We next consider a one-dimensional model for glacier growth [31]. The evolution of a glacier of height $u(x,t)$ resting upon a flat mountain can be described by the nonhomogeneous advection-diffusion equation

$$u_t + f(u)_x = D(\nu(u)u_x)_x + S(x,t,u),$$

where $D = 0.01$ and

$$f(u) = \frac{u + 3u^6}{4} \quad \text{and} \quad \nu(u) = 3u^6.$$

We take the initial condition

$$u(x,0) = \begin{cases} 1, & x < 0, \\ 0, & x > 0, \end{cases}$$

and the source term

$$S(x,t,u) = \begin{cases} S_0(x), & \text{if } u(x,t) > 0, \\ \max(S_0(x),0), & \text{if } u(x,t) = 0, \end{cases} \quad \text{where} \quad S_0(x) = \begin{cases} 0, & x < -0.4, \\ \frac{1}{2}(x+0.4), & -0.4 \le x \le -0.2, \\ -\frac{1}{2}x, & x > -0.2. \end{cases}$$

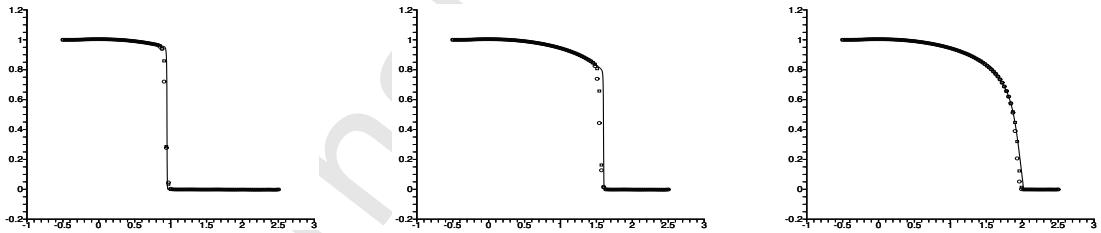

$t = 1$ $t = 2$ $t = 4$

Figure 19: Moving glacier on a uniform mesh of $M = 100$ elements at various times t. Circles show the explicit SSP2/WENO5/WENO-AO(4,3) scheme and squares show the explicit SSP3/WENO7/WENO-AO(6,4) scheme, using $\Delta t = 5h^2$ and $\Delta t = 6h^2$, respectively. The solid line is the reference solution (the latter scheme with $M = 800$).

For this example, we use uniform meshes of $M = 100$ elements and the explicit schemes that produce super-convergence. That is, we use SSP2/WENO5/WENO-AO(4,3) and SSP3/WENO7/WENO-AO(6,4). The numerical solutions are shown in Figure 19. They show good agreement with the reference solution using $M = 800$ (and the more accurate scheme). The sixth order scheme shows a bit better agreement than the fourth order scheme.

6.5. A strongly degenerate advection-diffusion equation

In our final set of tests, we consider a strongly degenerate parabolic advection-diffusion equation with a diffusion coefficient given by $D\nu(u)$, where

$$\nu(u) = \begin{cases} 0, & |u| \le 0.25, \\ 1, & |u| > 0.25, \end{cases} \tag{61}$$

and we take $D = 0.1$. The degeneracy is quite strong. In fact, our equation will be hyperbolic where $|u| \in [-0.25, 0.25]$ and parabolic elsewhere. We will take a Burgers flux.

6.5.1. A strongly degenerate advection-diffusion equation in 1D

The one dimensional equation is

$$u_t + f(u)_x - D(\nu(u)u_x)_x = 0.$$

We take $D = 0.1$, $f(u) = u^2$, and the Riemann initial condition

$$u(x,0) = \begin{cases} 1, & -\frac{1}{\sqrt{2}} - 0.4 < x < -\frac{1}{\sqrt{2}} + 0.4, \\ -1, & \frac{1}{\sqrt{2}} - 0.4 < x < \frac{1}{\sqrt{2}} + 0.4, \\ 0, & \text{otherwise}, \end{cases} \tag{62}$$

Results are shown in Figure 20.

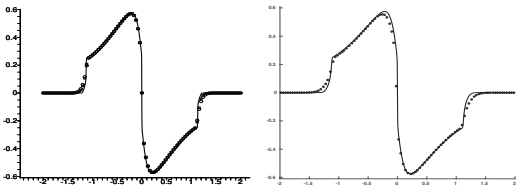

explicit schemes implicit Radau3-3-4

Figure 20: Burgers equation with a discontinuous diffusion coefficient (62) at time $t = 0.7$, using a mesh of $M = 100$ elements. Explicit results are on the left, using a uniform mesh, with circles for explicit SSP2/WENO5/WENO-AO(4,3) using $\Delta t = 3h^2$ and with squares for explicit SSP3/WENO7/WENO-AO(6,4) using $\Delta t = 4h^2$. The squares give a better solution than the circles. On the right are the results for implicit Radau3-3-4 using $\Delta t = 2h$ and non-uniform meshes. The solid lines are the reference solutions with $M = 800$ (explicit) and $M = 400$ (implicit).

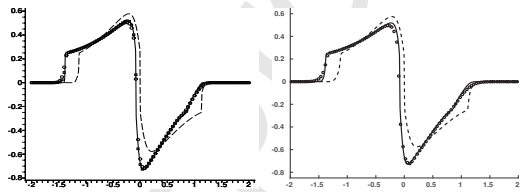

explicit schemes implicit Radau3-3-4

Figure 21: Burgers equation with an x-dependent discontinuous diffusion, $M = 100$, at $t = 0.7$. Explicit results are on the left, using a uniform mesh. Circles show explicit SSP2/WENO5/WENO-AO(4,3) using $\Delta t = 1.2h^2$, and squares show explicit SSP3/WENO7/WENO-AO(6,4) using $\Delta t = 1.5h^2$. On the right are the results for implicit Radau3-3-4 using $\Delta t = h$ and non-uniform meshes. The solid line is the reference solution using a fine mesh, and the dashed line is the x-independent diffusion solution from Figure 20.

We also compute solutions with an x-dependent diffusion $D\,\nu(x,u) = D\,(x - 1/\sqrt{2})^2\nu(u)$, where $\nu(u)$ is as (61). The results are shown in Figure 21, which shows that the solution is more diffusive when $x < 0$, as it should be, since $\nu(x,u)$ is bigger when $x < 0$. There is also a small advective effect due to the x-dependency of the diffusion coefficient, i.e., the overall flux from (6) is

$$f(u;x) = u^2 + 2D\,(x - 1/\sqrt{2})\,\nu(u).$$

6.5.2. A strongly degenerate advection-diffusion equation in 2D

Our final test considers the Burgers equation

$$u_t + \nabla F(u) - D\nabla\cdot(\nu(u)\nabla u) = 0, \quad F(u) = u^2\begin{pmatrix}1\\1\end{pmatrix}, \tag{63}$$

on $[-1.5, 1.5]^2$, where $D = 0.1$ and ν is defined in (61). The initial condition is

$$u(x,y,0) = \begin{cases} 1, & \text{if } (x+1/2)^2 + (y+1/2)^2 \le 0.16, \\ -1, & \text{if } (x-1/2)^2 + (y-1/2)^2 \le 0.16, \\ 0, & \text{otherwise.} \end{cases}$$

When the explicit and implicit schemes use $\Delta t = 2h^2$ and $\Delta t = 4h$, respectively, they give nearly identical plots. In Figure 22, we show a cross-section of both results at time $t = 0.5$. We also show the implicit result, for which the time step $\Delta t = 4h$. We believe we could obtain accurate results with an even longer time step, but our Newton solver is implemented in a naive way, and it breaks down for $\Delta t = 5h$.

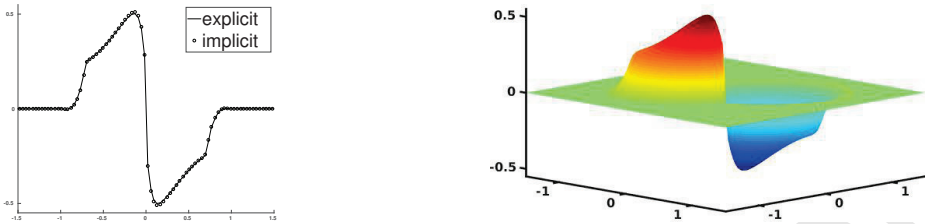

Figure 22: Burgers equation in 2D with a discontinuous diffusion coefficient. Solutions using $M = 80$ quadrilateral elements at time $t = 0.5$. A cross-section of the results for both the explicit ($\Delta t = 2h^2$) and implicit ($\Delta t = 4h$) schemes (left), and the implicit solution (right).

7. Summary and Conclusions

We considered numerical approximation of the degenerate advection-diffusion equation. We developed both explicit and implicit finite volume weighted essentially non-oscillatory (WENO) schemes for this possibly degenerate equation, which may exhibit parabolic or hyperbolic behavior. The diffusion was reformulated through the use of the Kirchhoff transformation to better handle the degeneracy. We presented in detail schemes that are third order in both space and time in one and two space dimensions using non-uniform meshes in 1D and meshes of quadrilaterals in 2D.

We used WENO-AO reconstructions for the spatial discretization. Classic WENO achieves higher order accuracy by special (linear) weighting of the smaller stencil polynomials. These linear weights may not exist or they may be negative. WENO-AO achieves higher order accuracy by incorporating the polynomial of the larger stencil, and thus the linear weights are arbitrarily set by the user; that is, they always exist and they can be taken to be positive. Moreover, because there are no special linear weights, non-uniform and irregular computational meshes can be handled in a natural way. In two space dimensions, we presented a reconstruction technique that is well-suited for logically rectangular meshes, using tensor product polynomials so that there is a match between the number of polynomial unknowns and the number of elements in the stencil.

We developed a special two-stage reconstruction procedure to handle degenerate diffusion. We used WENO-AO to reconstruct the solution from its element averages $\bar{u}$. This reconstruction gives point values of the solution u, which in turn give point values for the Kirchhoff variable $b(u)$. Finally, these are reconstructed into a stencil polynomial, and several of these are combined as in the WENO methodology using smoothness indicators.

Time was discretized using the method of lines and a Runge-Kutta time integrator. We used Strong Stability Preserving (SSP) Runge-Kutta methods for the explicit schemes. Stability requires a severe parabolically scaled time step restriction $\Delta t = O(h^2)$. We also used implicit Runge-Kutta methods. Because SSP methods are only conditionally stable, we turned to L-stable Runge-Kutta methods, which can handle the stiff diffusive components of the problem. For a third order scheme, we used Radau IIA Runge-Kutta. We showed that the overall implicit scheme is unconditionally L-stable on uniform computational meshes for smooth solutions to the linear problem, through a von Neumann (or Fourier mode) stability analysis.

Computational results showed the ability of the schemes to accurately approximate challenging test problems. We showed that the schemes are third order in general, and exhibit superconvergence on uniform meshes (if the time stepping and handling of the advective terms is accurate enough). We showed that the implicit scheme using Radau IIA is comparable to the use of a third order implicit SSP Runge-Kutta method when the time step is within the stability region, and that Radau IIA is superior to implicit SSP outside the stability region. In other words, our scheme is more robust to the choice of time step. The schemes produced accurate solutions for the porous medium equation, Burgers equation, and Buckley-Leverett problems in 1D and 2D on non-uniform meshes, with the implicit scheme using the reasonable hyperbolically scaled $\Delta t = O(h)$.

The schemes of [2, 3] are of the finite difference variety, use explicit time-stepping only, and they require uniform computational meshes. The scheme of [4] requires specially structured equations and rectangular meshes, and uses explicit time-stepping and is only second order accurate. It appears that our schemes are the first high order, general purpose finite volume WENO schemes developed for the degenerate advection-diffusion equation. They can use explicit or implicit time stepping, and they use non-uniform computational meshes in multiple space dimensions.

Acknowledgements

The research of Todd Arbogast was supported in part by U.S. National Science Foundation grant DMS-1720349. The research of Chieh-Sen Huang was supported in part by the Taiwan Ministry of Science and Technology grant MOST 107-2115-M-110-004-MY2, the Multidisciplinary and Data Science Research Center of the National Sun Yat-sen University, and the National Center for Theoretical Sciences, Taiwan.

References

[1] T. Arbogast, M. F. Wheeler, N.-Y. Zhang, A nonlinear mixed finite element method for a degenerate parabolic equation arising in flow in porous media, SIAM J. Numer. Anal. 33 (1996) 1669–1687.
[2] Y. Liu, C.-W. Shu, M. Zhang, High order finite difference weno schemes for nonlinear degenerate parabolic equations, SIAM Journal on Scientific Computing 33 (2) (2011) 939–965.
[3] R. Abedian, H. Adibi, M. Dehghan, A high-order weighted essentially non-oscillatory (WENO) finite difference scheme for nonlinear degenerate parabolic equations, Computer Physics Communications 184 (2013) 1874–1888.
[4] M. Bessemoulin-Chatard, F. Filbet, A finite volume scheme for nonlinear degenerate parabolic equations, SIAM J. SCI. COMPUT. 34 (5) (2012) B559–B583.
[5] D. Levy, G. Puppo, G. Russo, Compact central WENO schemes for multidimensional conservation laws, SIAM J. Sci. Comput. 22 (2) (2000) 656–672.
[6] D. S. Balsara, S. Garain, C.-W. Shu, An efficient class of WENO schemes with adaptive order, J. Comput. Phys. 326 (2016) 780–804.
[7] T. Arbogast, C.-S. Huang, X. Zhao, Accuracy of WENO and adaptive order WENO reconstructions for solving conservation laws, SIAM J. Numer. Anal. 56 (3) (2018) 1818–1847, DOI 10.1137/17M1154758.
[8] I. Cravero, G. Puppo, M. Semplice, G. Visconti, CWENO: Uniformly accurate reconstructions for balance laws, Math. Comp.doi:10.1090/mcom/3273.
[9] C.-W. Shu, Total-variation-diminishing time discretizations, SIAM J. Sci. Statist. Comput. 9 (1988) 1073–1084.
[10] C.-W. Shu, S. Osher, Efficient implementation of essentially non-oscillatory shock capturing schemes, J. Comput. Phys. 77 (1988) 439–471.
[11] S. Gottlieb, C.-W. Shu, E. Tadmor, Strong stability preserving high-order time discretization methods, SIAM Review 43 (2001) 73–85.
[12] S. Gottlieb, On high order strong stability preserving Runge-Kutta and multi step time discretizations, J. Sci. Comput. 25 (1–2) (2005) 105–128. doi:DOI: 10.1007/s10915-004-4635-5.
[13] D. I. Ketcheson, C. B. Macdonald, S. Gottlieb, Optimal implicit strong stability preserving Runge-Kutta methods, Applied Numerical Mathematics 59 (2009) 373–392.
[14] E. Hairer, G. Wanner, Solving ordinary differential equations II: Stiff and differential-algebraic problems, 2nd Edition, Springer-Verlag, Berlin, New York, 1996.
[15] E. Hairer, C. Lubich, G. Wanner, Geometric Numerical Integration: Structure-Preserving Algorithms for Ordinary Differential Equations, 2nd Edition, Springer-Verlag, Berlin, New York, 2006.
[16] G.-S. Jiang, C.-W. Shu, Efficient implementation of weighted ENO schemes, J. Comput. Phys. 126 (1996) 202–228.
[17] C.-W. Shu, Essentially non-oscillatory and weighted essentially non-oscillatory schemes for hyperbolic conservation laws, Tech. Rep. ICASE Report no. 97–65, National Aeronautics and Space Administration, Langley Research Center, Hampton, Virginia (November 1997).
[18] O. Friedrich, Weighted essentially non-oscillatory schemes for the interpolation of mean values on unstructured grids, J. Comput. Phys. 144 (1998) 194–212.
[19] C. Hu, C.-W. Shu, Weighted essentially non-oscillatory schemes on triangular meshes, J. Comput. Phys. 150 (1999) 97–127.
[20] V. A. Titarev, P. Tsoutsanis, D. Drikakis, WENO schemes for mixed-element unstructured meshes, Commun. Comput. Phys. 8 (2010) 585–609.
[21] M. Dumbser, M. Käser, Arbitrary high order non-oscillatory finite volume schemes on unstructured meshes for linear hyperbolic systems, J. Comput. Phys. 221 (2007) 693–723.
[22] Y.-T. Zhang, C.-W. Shu, Third order WENO scheme on three dimensional tetrahedral meshes, Commun. Comput. Phys. 5 (2009) 836–848.
[23] T. Arbogast, C.-S. Huang, X. Zhao, Von Neumann stable, implicit, high order, finite volume WENO schemes, in: SPE Reservoir Simulation Conference 2019, Society of Petroleum Engineers, Galveston, Texas, 2019, p. to appear, sPE-193817-MS.
[24] F. Aràndiga, A. Baeza, A. M. Belda, P. Mulet, Analysis of WENO schemes for full and global accuracy, SIAM J. Numer. Anal. 49 (2) (2011) 893–915.
[25] D. W. Peaceman, Fundamentals of numerical reservoir simulation, Elsevier, Amsterdam, 1977.
[26] J. C. Strikwerda, Finite Difference Schemes and Partial Differential Equations, 2nd Edition, SIAM, Philadelphia, 2004.
[27] G. B. Folland, Introduction to Partial Differential Equations, Princeton, 1995.
[28] A. Kurganov, E. Tadmor, New high-resolution central schemes for nonlinear conservation laws and convection-diffusion equations, J. Comput. Phys. 160 (2000) 241–282. doi:DOI 10.1006/jcph.2000.6459.
[29] Q. Zhang, Z.-L. Wu, Numerical simulation for porous medium equation by local discontinuous Galerkin finite element method, Journal of Scientific Computing 38 (2) (2009) 127–148. doi:10.1007/s10915-008-9223-7.
URL https://doi.org/10.1007/s10915-008-9223-7
[30] G. I. Barenblatt, On self-similar motions of compressible fluids in porous media, Prikl. Mat. Mekh. 16 (6) (1952) 679–698, in Russian.
[31] A. C. Flower, Glaciers and ice sheets, in: J. I. Diaz (Ed.), The Mathematics of Models for Climatology and Environment, Vol. 48 of NATO ASI subseries I, Springer-Verlag, 1997, pp. 301–336.

Declaration of interests

☒ The authors declare that they have no known competing financial interests or personal relationships that could have appeared to influence the work reported in this paper.

☐The authors declare the following financial interests/personal relationships which may be considered as potential competing interests: